CZECH TECHNICAL UNIVERSITY IN PRAGUE

FACULTY OF BIOMEDICAL ENGINEERING
Department of Biomedical Technology

A COMPUTATIONAL BIOMECHANICS STUDY OF THE SPINAL CORD IN PATIENTS WITH CHIARI MALFORMATION AND SYRINGOMYELIA

Master thesis

Study programme: Biomedical and Clinical Technology

Study branch: Biomedical Engineering

Author of the master thesis: Ing. Asawari Pratiksha Ashok Kumbhar

Supervisor of the master thesis: doc. Ing. Martin Rožánek, Ph.D.

Kladno, May 2021

I. Personal and study details

Student's name: **Kumbhar Asawari Pratiksha Ashok**   Personal ID number: **488082**

Faculty / Institute: **Faculty of Biomedical Engineering**

Department / Institute: **Department of Biomedical Technology**

Study program: **Biomedical and Clinical Technology**

Branch of study: **Biomedical Engineering**

II. Master's thesis details

Master's thesis title in English:

A computational biomechanics study of the Chiari-Syringomyelia complex - Mechanics of Spinal Cord

Master's thesis title in Czech:

Biomechanická studie Syringomyelie s Chiariho malformací - mechanika míchy

Guidelines:

Bibliography / sources:

[1] Christian Constanda, Matteo Dalla Riva, Pier Domenico Lamberti, Integral Methods in Science and Engineering Volume 2 Practical Applications, ed. 1, Birkh user, 2017, ISBN 978-3-319-16727-5.
[2] C. D. Bertram , M. Heil , A Poroelastic Fluid/Structure-Interaction Model of Cerebrospinal Fluid Dynamics in the Cord With Syringomyelia and Adjacent Subarachnoid-Space Stenosis, J Biomech Eng, ročník 139, číslo 1, 2017.
[3] N. S. J. Elliott , D. A. Lockerby , A. R. Brodbelt , The Pathogenesis of Syringomyelia: A Re-Evaluation of the Elastic-Jump Hypothesis, J Biomech Eng, ročník 131, číslo 4, 2009.

Name and workplace of master's thesis supervisor:

doc. Ing. Martin Rožánek, Ph.D.,   Department of Biomedical Technology,   FBME

Name and workplace of second master's thesis supervisor or consultant:

Date of master's thesis assignment: **10.02.2020**   Deadline for master's thesis submission: **13.08.2020**

Assignment valid until: **19.09.2021**

_____
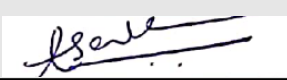doc. Ing. Martin Rožánek, Ph.D.
Supervisor's signature

_____
Head of department's signature

_____
prof. MUDr. Ivan Dylevský, DrSc.
Dean's signature

III. Assignment receipt

_____
Date of assignment receipt

_____
Student's signature

DECLARATION

I hereby declare that I have completed this thesis with the topic "A computational biomechanics study of the spinal cord in patients with Chiari malformation and Syringomyelia" independently, and that I have attached an exhaustive list of citations of the employed sources.

I do not have a compelling reason against the use of the thesis within the meaning of Section 60 of the Act No. 121/2000 Sb., on copyright, rights related to copyright and amending some laws (Copyright Act).

In Kladno May 2021   Asawari Pratiksha Ashok Kumbhar, MSc.

Master's Thesis title:

A computational biomechanics study of the spinal cord in patients with Chiari malformation and Syringomyelia

Abstract

The pathogenesis of syringomyelia in association with Chiari malformation (CM) is unclear. The mechanical properties of solid tissues and cerebrospinal fluid flow have been shown to contribute to the development of syrinx. This thesis aims to study the biomechanical behavior of the spinal cord in the aforementioned diseased condition. A 2D axis-symmetric poroelastic model of the spinal cord in the presence of syringomyelia was developed to understand the flow dynamics in porous solids. An arterial pressure pulse of 500 Pa was applied at the cranial end of the subarachnoid space. Transient excitation gave rise to wave propagation in the fluid-filled subarachnoid space. The main effect of the excitation was compression and swelling of spinal cord tissue at the syrinx level at different pressure conditions. The velocities of fluid entering and leaving the syrinx were relatively low i.e., in the range of 10^{-5} m/s such that the porous spinal cord absorbing the fluid. Stresses induced in pia mater were larger at the level of syrinx as compared to the rest of the model geometry. Although poroelasticity gives a major insight into the material interaction with fluid in a porous media, it lacks the complexities involved in free flow equations which are more realistic to determine the behavior of biological tissue. An extension to the existing model with the fluid-structure interaction module was built to study the effect of the free-flow zone connected to the poroelastic media.

Key words:

Chiari Malformation; syringomyelia; cerebrospinal fluid; poro-elasticity; biomechanics

Název diplomové práce:

Biomechanická studie Syringomyelie s Chiariho malformací - mechanika míchy

Abstrakt:

Patogeneze syringomyelie ve spojení s Chiariho malformací (CM) je nejasná. Bylo prokázáno, že mechanické vlastnosti pevných tkání a toku mozkomíšního moku přispívají k rozvoji syrinxu. Tato práce si klade za cíl studovat biomechanické chování míchy ve výše uvedeném chorobném stavu. Pro pochopení dynamiky toku v porézních pevných látkách byl vyvinut 2D osově symetrický poroelastický model míchy v přítomnosti syringomyelie. Na lebeční konec subarachnoidálního prostoru byl aplikován puls arteriálního tlaku 500 Pa. Přechodná excitace vedla k šíření vln v kapalinou naplněném subarachnoidálním prostoru. Hlavním účinkem excitace byla komprese a otok tkáně míchy na úrovni syrinx za různých tlakových podmínek. Rychlosti tekutiny vstupující a vystupující ze syrinxu byly relativně nízké, tj. V rozmezí 10^{-5} m/s, takže porézní mícha absorbující tekutinu. Stresy indukované v pia mater byly větší na úrovni syrinxu ve srovnání se zbytkem geometrie modelu. Ačkoli poroelasticita poskytuje hlavní pohled na interakci materiálu s tekutinou v porézním médiu, postrádají složitosti rovnic volného toku, které jsou realističtější pro určení chování biologické tkáně. Bylo vytvořeno rozšíření stávajícího modelu s modulem interakce tekutina-struktura, aby se studoval účinek zóny volného toku připojené k poroelastickému médiu.

Klíčová slova:

Chiariho malformace; syringomyelia; mozkomíšní mok; poro-pružnost; biomechanika

Acknowledgments

I wish to express my sincere appreciation to my supervisor, Professor Martin Rožánek, who convincingly guided and encouraged me to complete the thesis work. I would like to express my gratitude and appreciation for Professor Patrick Segers and dr. Frank Dewaele, Ghent University, Belgium. The guidance, support, and encouragement from them have been invaluable throughout this study.

Lastly, I wish to acknowledge the support and great love of my family and friends. They kept me going on and this work would not have been possible without their input.

Table of Contents

List of Figures

List of Abbreviations

CNS   **Central Nervous System**

CSF   **Cerebrospinal Fluid**

SAS   **Subarachnoid Space**

SAT   **Subarachnoid Trabeculae**

PAC   **Pia-Arachnoid Complex**

CM   **Chiari malformation**

PFD   **Posterior Fossa Decompression**

PC-MRI   **Phase Contrast Magnetic Resonance Imaging**

CFD   **Computational Fluid Dynamics**

FSI   **Fluid-Structure Interaction**

List of Symbols

$\mathbf{u}$ Darcy velocity (m/s)

$\mathbf{\kappa}$ Permeability of the porous medium (m^2)

$\mathbf{\mu}$ Fluid's dynamic viscosity (Pa·s)

$\mathbf{p}$ Fluid's pressure (Pa)

$\mathbf{\rho}$ Density (kg/m^3)

$\mathbf{g}$ Magnitude of gravitational acceleration (m/s^2)

$\mathbf{\nabla D}$ Unit vector

$\mathbf{\varepsilon}$ Porosity,

$\mathbf{Q_m}$ Mass source term (kg/(m^3·s)

$\mathbf{E}$ Young's modulus (Pa)

$\mathbf{\sigma}$ Poisson's ratio

1. Introduction

1.1 Anatomy and Physiology of the Central Nervous System

Syringomyelia is a rare neurological condition that causes the formation of fluid-filled cavities (also called Syrinxes) in the spinal cord tissue. The mean prevalence of MRI-confirmed syringomyelia ranges, in different countries, between 2 and 13 per 100,000 inhabitants. Syringomyelia accounts for about 5% of paraplegias which causes impairment in motor or sensory functions of lower extremities (1) (2).

The causes of syringomyelia vary from traumatic spinal cord injury to certain neurological disorders such as Chiari Malformation (CM) type 1. CM1 comprises the common abnormality encountered at the craniovertebral junction and subsequently abnormal flow of the CSF into the spinal cord which predominates the cause of the syringomyelia (3). Current research on the mechanics of the syrinx formation focuses on the interaction of spinal cord tissue with the CSF (4). As mathematical modeling of biological tissues gives a more sophisticated way to examine the underlying mechanisms than monitoring the patient with the symptoms. It has become a popular method to simulate the environment in which the syrinx develops in the tissue.

The Central nervous system (CNS) of the body consists of the brain and spinal cord.

1.1.1 Anatomy of the Brain

The brain is protected by the skull and different layers of meninges, namely the pia, the arachnoid, and the dura. The innermost layer is the pia mater, which is in close contact with the brain surface. The middle layer, arachnoid mater is a thin, transparent membrane that is also thought to be impermeable to fluids. The space between the pia and arachnoid is the subarachnoid space (SAS) which contains the CSF. It is a clear, colorless liquid produced from arterial blood by the choroid plexuses, as shown in Figure 1, (5). The main function of CSF is hydromechanical protection of the central nervous system. It plays a vital role in brain development and regulation of brain interstitial fluid homeostasis (6).

The brain is composed of three main parts namely, cerebellum, cerebrum, and brain stem as seen in Figure 1.
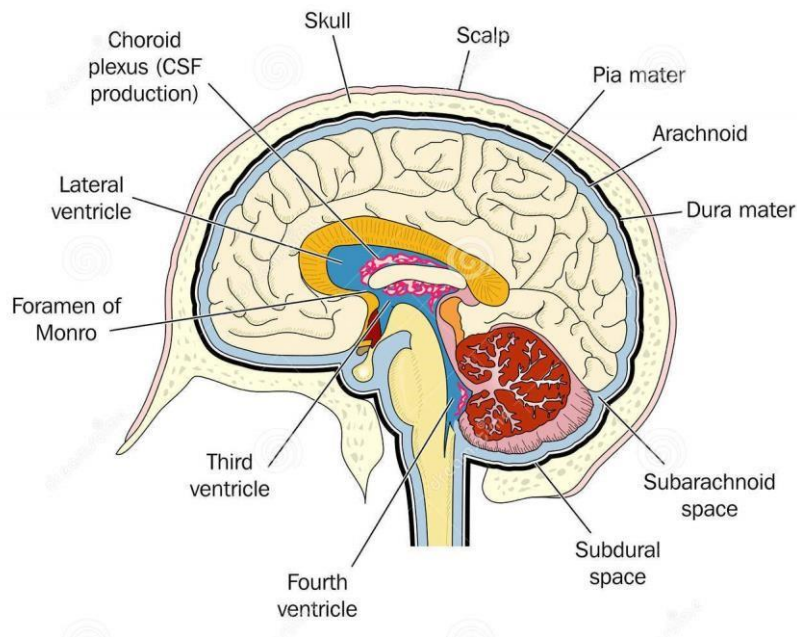
Figure 1 Sagittal view of the human brain (5)

1.1.1.1 Cerebrum

Of the three basic divisions of the brain, the cerebrum is the largest part and consists of two hemispheres and layers of neural tissue, named cortices. The outer layer of the cortex is made up of grey matter and the underlying layer is the white matte, as shown in Figure 2. The properties of grey and white matter vary to a microstructural level depending upon the neural structures each layer is made up of.

The CNS is comprised of a variety of neuronal tissue and cell bodies. Nervous tissue contains two major cell types, neurons and glial. Neurons are polarized cells that transmit signals in the form of electric current along the membrane. Signals are received at the dendrites, are passed along the cell body, and propagate along the axon towards the receptor or target. Many axons are shielded with a lipid-rich substance called myelin and hence, the axons are myelinated. Glial cells are divided based on the anatomical division in which they are found. The main functions of glial cells are maintaining the chemical environment around the neuron and provide insulation to neurons.

Structures such as dendrites, cell bodies, and unmyelinated axons make up the grey matter. While the inner core of white matter consists of myelinated axons making it stiffer than the grey matter (7). The variation in the microstructure of white and grey matter decides the mechanical properties of the tissue. The morphological structure of grey mater consists of randomly oriented cell bodies and axons making it isotropic material than the white matter (8). The main functions are controlled by cerebrum such as interpreting touch, vision, and hearing, as well as speech, reasoning, emotions, learning, and fine movement control (5).
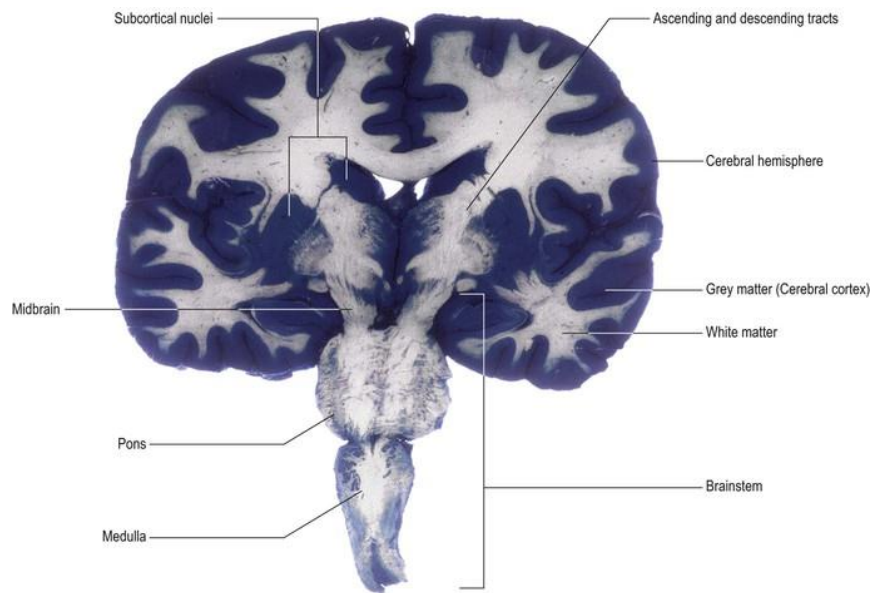
Figure 2 Coronal section through the brain showing the stained grey matter and white matter of cerebrum (5)

1.1.1.2 Cerebellum

The cerebellum is located at the base of the cerebrum consisting of two lateral hemispheres connected by a medial part called vermis, as depicted in Figure 3. Each hemisphere has an ovoid lobule, named as cerebellar tonsil, situated posteriorly. The cerebellum is connected to the brainstem by fiber bundles that connect it to medulla, pons, and midbrain. It overlies the fourth ventricle. The cerebellum consists of an outer layer of grey matter and an inner core of the white matter, as shown in Figure 4. The main function of the cerebellum is motor control such as maintenance of equilibrium, posture and muscle tone, and movement coordination (5).
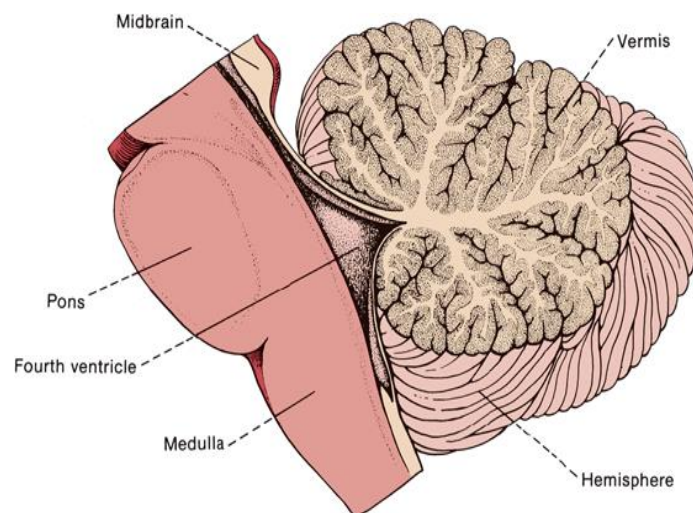
Figure 3. Coronal section through the brain at the midbrain and hindbrain level (9)
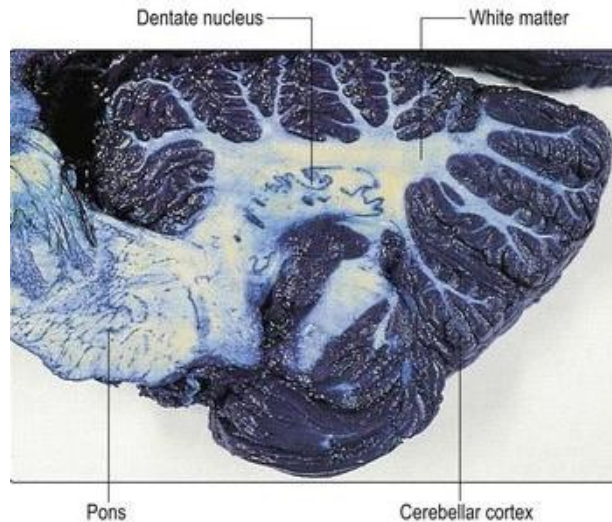
Figure 4 Coronal section through the brain showing the stained grey matter and white matter of cerebellum (5)

1.1.1.3 Brainstem

The brain stem consists of the medulla, pons, and midbrain (Figure 3). It is dorsally (from the tip of the nose towards the back of the head) covered by the cerebellum and sits at the back of the skull. It is a bulb-shaped structure that has nerve fibers originating from or terminating in, from various anatomical structures. The medulla continues to form the spinal cord from foramen magnum (hole in the base of the skull) in caudal (away from the brain) direction. The floor of the medulla forms the fourth ventricle, which is a shallow, diamond-shaped depression. The brainstem has numerous cranial nerve nuclei and is a passageway to many important neural networks. It acts like an intermediary connecting the spinal cord to the higher centers of the forebrain. The brain stem controls the flow of messages between the brain and the rest of the body. It also controls basic body functions such as breathing, swallowing, heart rate, blood pressure, consciousness, and whether one is awake or sleep (5).

1.1.2 Anatomy of the Spinal Cord

The spinal cord is enclosed in the vertebral canal of the vertebral column that provides protection and support. The spinal cord originates from the brain stem as a continuation of the medulla. It is a segmental structure from cranial to caudal, it consists of 8 cervical, 12 thoracic, 5 lumbar, 5 sacral, and 1 coccygeal segment (Figure 5). The cord is approximately cylindrical with varying dimensions at different segments. It enlarges at the cervical and lumbar segment and tapers from the lumber region in caudal direction to form a conical termination. The spinal cord has 31 bilaterally paired spinal nerves, each pair associated with the corresponding cord segment (5). The spinal nerves are mixed nerves that carry sensory, motor, and autonomic signals between the brain and spinal cord. Afferent sensory axons are transmission lines from the body to the spinal cord and brain through the dorsal (posterior) root of the spinal cord as shown in figure 5. They carry the sensory information along the transmission line. Similarly, efferent motor axons are transmission lines from the brain to the body through the

ventral(anterior) roots of the spinal cord as shown in Figure 6. They bring motor information along the transmission line (9).
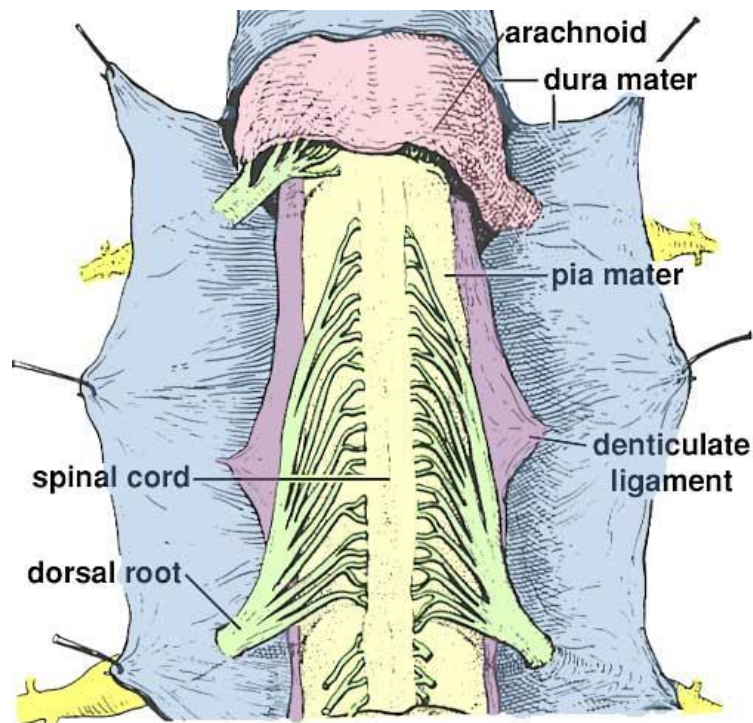
Figure 5 Layers of meninges in the spinal cord (10)

The spinal cord, like the brain, has three concentric meningeal covering: the pia mater, arachnoid mater, and dura mater. The main functions of the spinal cord are to carry signals from the brain to the whole body and vice versa, transmit nerve reflex response for movement, sensation, pressure, temperature, and many more (9).

1.1.2.1 Spinal meninges

The innermost covering is the pia mater, which is delicate, the vascular membrane of microscopic thickness about 150-200 µm, that is closely employed to the surface of cords and nerve roots. It contains flat overlapping pial cells with an oval-shaped nucleus. Aligned centrally between the dorsal and ventral roots of spinal nerves is attached to a membranous continuation of pia called denticulate ligament (Figure 5).
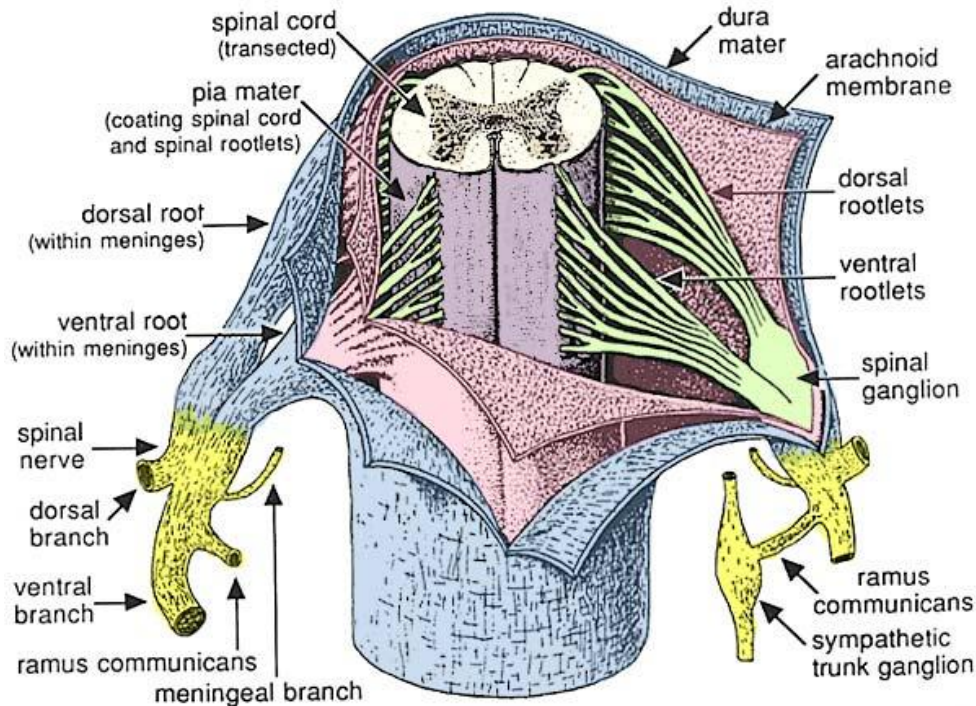
Figure 6 Ventral and dorsal aspect of the spinal cord, showing the relationships of the spinal nerve roots and the meninges (10)

The arachnoid mater lies between pia and dura. It is a thin, translucent membrane that has a spiderweb-like appearance. The intermittent lateral projections of the denticulate ligament tether the spinal cord to arachnoid mater and through it to dura mater. Between pia and arachnoid mater, lies the SAS which contains CSF from the ventricular system of the brain. The outermost covering of the spinal cord is the dura mater. It is a tough, fibrous membrane that envelops the cord loosely. The arachnoid mater is in close contact with the dura but separated by a theoretical plane called the subdural space. The dura mater is separated from the vertebral column by epidural space *(5)*. The epidural space contains fat, veins, arteries, spinal nerve roots, and lymphatics. The internal venous plexus, formed from intraspinal veins, is situated in the epidural space which extends in length throughout the spinal cord till the Foramen magnum. At this point, it forms a dense network that communicates with the vertebral veins *(10)*.

Although the spinal cord terminates at the vertebral level of the lumbar region, the arachnoid and dura along with the SAS continue caudally up to the sacral region (Figure 7) (5).

1.1.2.2 Internal structure of the spinal cord

The spinal cord is incompletely divided into two symmetrical halves. In the center lies the small central canal, which continues with the ventricular system. The spinal cord tissue(parenchyma) consists of two types of layers i.e., grey, and white matter. Around the central canal lies grey matter, consisting of nerve cell bodies and synaptic connections. The outermost part of the spinal cord is made up of white matter, which

contains ascending and descending nerve fibers. Different levels of cord segments vary in volume and pattern of grey and white matter.
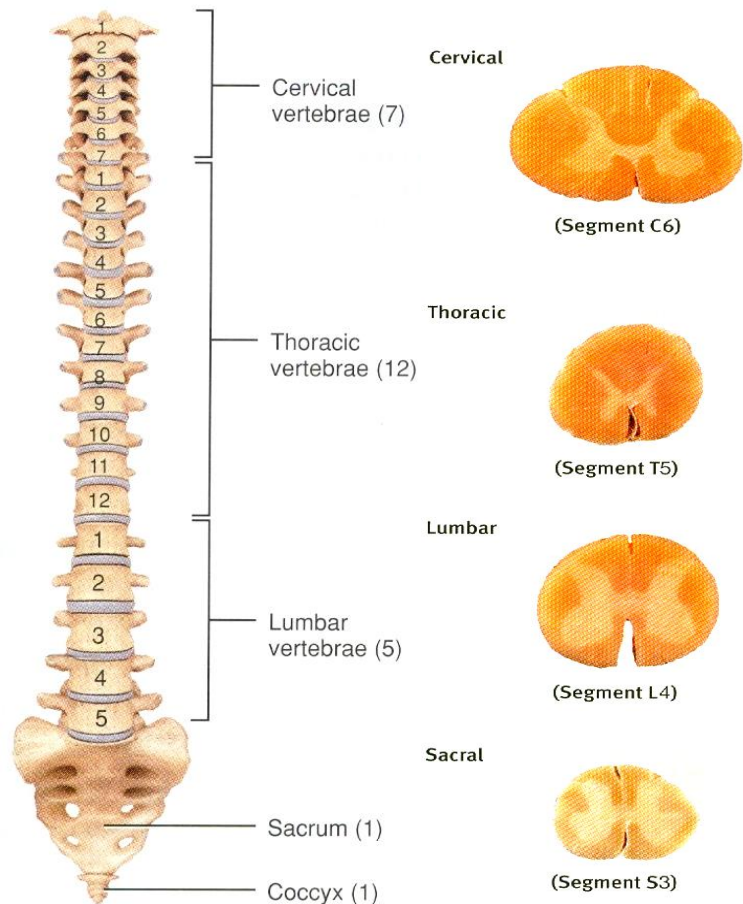
Figure 7 Location of spinal cord regions and the corresponding shapes of grey and white matter in the cord cross-section (12)

1.1.2.2.1 Grey matter of the spinal cord:

The grey matter, transversely butterfly-shaped structure, is divided into four columns: dorsal horn, ventral horn, intermediate column, lateral horn. The dorsal horn contains neurons that receive sensory information from the body to the brain. The intermediate column and lateral horn contain neurons from the visceral and pelvic organs. The ventral horn contains motor neurons from the spinal cord to the skeletal muscle (11). Glial cells are also found in the grey matter, providing nourishment and energy to neurons. As the axons are not myelin coated, it gives the greyish hue to the tissue (12).

1.1.2.2.2 White matter of the spinal cord:

White matter is mainly composed of long-range myelinated axons (that transmit signals to the grey matter) and very few neuronal cell bodies. As it is myelin-dense nervous tissue, therefore it is whitish. The structural anatomy plays a vital role in the mechanical properties of the spinal cord tissue. Hence the difference in cell bodies between the grey and white matter determine the local mechanical properties such as elasticity, permeability, etc. (12).

1.1.2.2.3 Perivascular spaces in grey and white matter:

The fluid exchange between the spinal cord parenchyma or brain tissue and surrounding SASs, where the CSF circulates, is carried out by perivascular spaces in the tissue. The ultramicroscopic investigation as shown in Figure 8 and Figure 9, of the spinal cord tissue indicates perivascular spaces related to all arterioles and venules, throughout the white matter and central grey matter (13). An artery in the SAS has a complete internal layer of elastic tissue and a coat of smooth muscle. It is surrounded by pial cells which are continuous with the pia mater. The thin single-layered covering of pia mater provides a subarachnoid arteriole and is separated from the smooth muscle coat of the vessel by a thin layer of collagenous connective tissue consequently forming small pores or gaps in the pial coating (14).

The discontinuity of pia and arachnoid layers allows CSF to move through the SAS and enter the perivascular spaces. In spinal cord parenchyma, perivascular spaces are continuous with the extracellular spaces of the surrounding tissue (Figure 10). This anatomical continuity provides low resistance to the flow of CSF in the tissue (13).
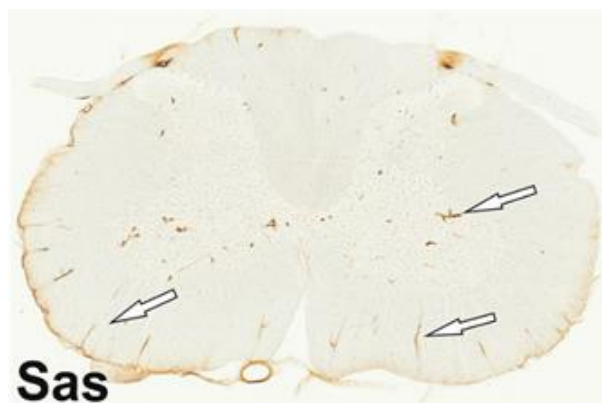
Figure 8 Cervical spinal cord transverse section stained with DAB and H2O2 (15)
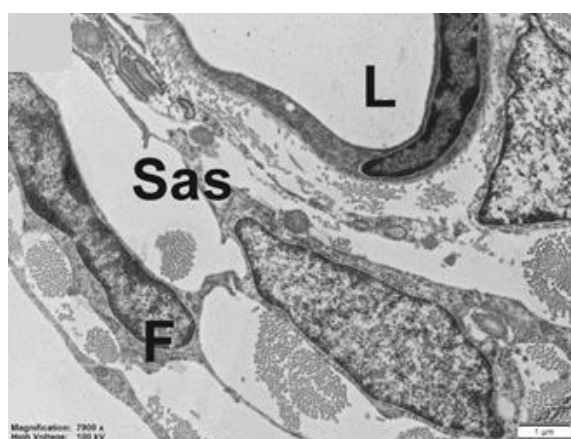
Figure 9 with venule (L: lumen of a blood vessel) embedded in fibroblast(F) and collagen fibers (15).

Figure 10. Perivascular spaces as a proposed pathway for CSF flow. Flow from the SAS enters the perivascular spaces, which narrows as they penetrate deeper into the cord (15)

1.1.2.2.4 Arachnoid Trabeculae:

The arachnoid trabeculae are a network of collagen fibers situated between the arachnoid and pia mater. The SAS is a complex structure as it encompasses the trabeculae along with the CSF flow. This is due to the presence of rod-shaped trabeculae, extended from arachnoid mater to the pia mater in a tree form (Figure 11)
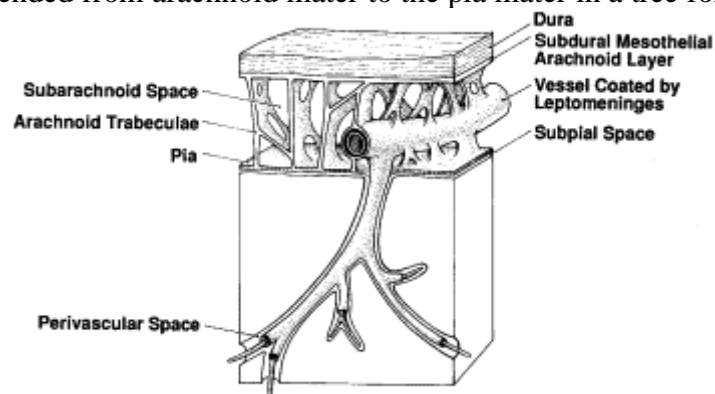
Figure 11 The drawing depicting the relationship between dura, arachnoid, and pia with emphasis on the arachnoid trabeculae (16)

The literature and knowledge about the anatomical distribution of the spinal arachnoid trabeculae are confined. According to Rickenbacher et al. (17), the orientation of the trabeculae varies along the length of the spinal SAS. The upper cervical region consists of few trabeculae while the lower cervical region consists of an incomplete membranous expansion of fibers (Figure 12). In the thoracic region, these trabeculae fibers form a membrane running anteroinferior with perforations on the surface. Towards the extremity, the trabeculae become scant along the course. It gives shape to tubular arachnoid sheaths for each nerve root and consequently the spinal cord.
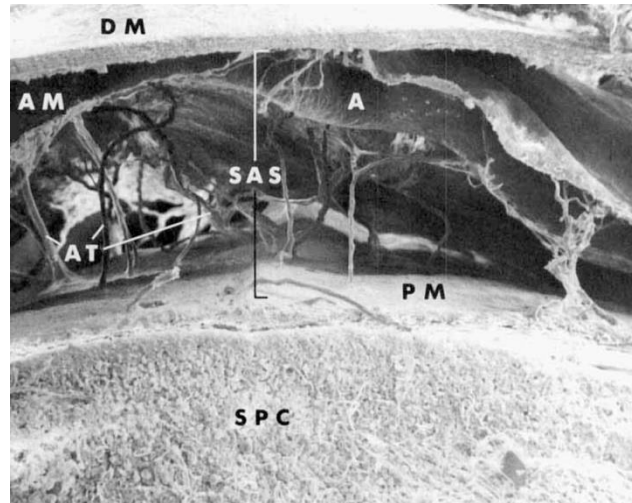
Figure 12 Spinal meninges and SAS with arachnoid trabeculae (AT); pia mater (PM); arachnoid mater (AM); spinal cord (SPC); artery(A); dura mater (DM), observed under an electron microscope (18)

Based on a study by Killer et al. (19), subarachnoid trabeculae (SAT) also called as pia-arachnoid complex (PAC), plays an important role as mechanical pillars between the pia and arachnoid mater, damping and restricting the movement of brain and spinal cord relative to the skull and vertebral column respectively (Figure 11). The interaction between the CSF and the trabeculae mechanically supports the brain and the spinal cord (16). A finite element model by Scott et al. (18), explains the significant effect of the PAC on the brain and spinal cord biomechanics and the mechanism that explains the increasing local variability of stress along the CNS.

1.1.2.3 Filum Terminale

The filum terminale is a modification of pia mater from the sacral region to the extremity of the spinal cord (Figure 13). It is fibrous tissue including glial cells, connective tissue, and remnants of an ependymal-lined central canal. It provides longitudinal support to the spinal cord tissue (20). Ultrastructural studies have demonstrated an abundance of collagen and elastin fibers making it denser than the spinal cord (21)
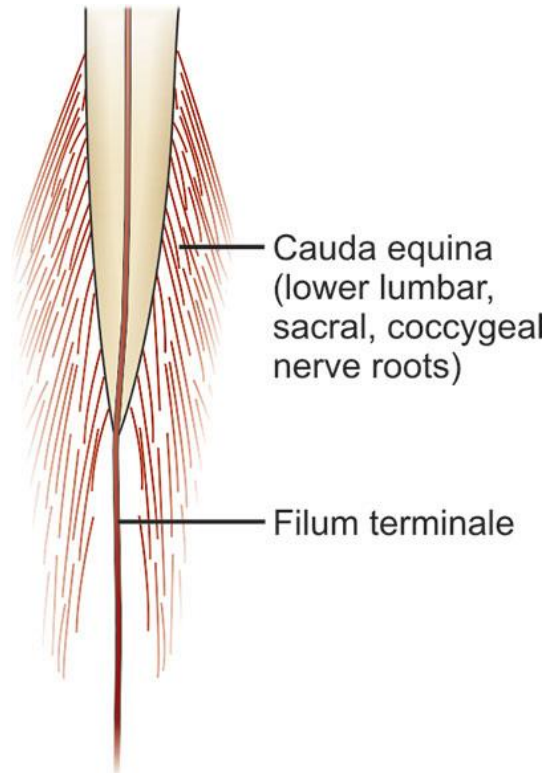
Figure 13 The filum terminale (21)

1.1.3 Flow of CSF in the spinal cord

The CSF flows from the sites of production to the sites of absorption in bulk quantities. The flow is bidirectional in the spinal cord. It is primarily secreted by choroid plexus in the ventricles at a rate of 500 ml/day. CSF has a viscosity close to that of water and is distributed in three spaces that communicate with each other, the cerebral ventricles, and the cranial and spinal SASs. The value of the viscosity of CSF at 37°C is in the range of 0.7–1 mPa·s (22).

The choroid plexus is a specialized epithelial tissue called ependyma, that forms lining in all the ventricles of the brain and cerebral aqueduct. CSF production takes place employing the ependymal cells. The tight junction of the ependymal cells forms the blood-CSF barrier along with the arachnoid mater to create a pair of membranes that separate the blood from the CSF. The choroidal arteries at various anatomical locations supply blood to the choroid plexus at various levels (Figure 14) (23).

Fluid formed in the lateral ventricles flows through a narrow opening called the foramen of Monroe into the third ventricle, then through the aqueduct of Sylvius into the fourth ventricle. Majority of the CSF transmitted in the fourth ventricle flows into the SAS; a small amount of may enter the central canal of the spinal cord (5) CSF has shown to flow from the spinal SAS into the spinal perivascular areas, across the interstitial space, then into the central canal. As the fluid enters the SAS, it flows down the spinal cord or flows up over the cortical structures, eventually to the secretion sites. The flow is prominently superimposed by the pulsatile motion due to the beating of the heart.

During the systole, the brain expands inwards compressing the ventricles and outwards, compressing the SAS (Figure 15) (24).
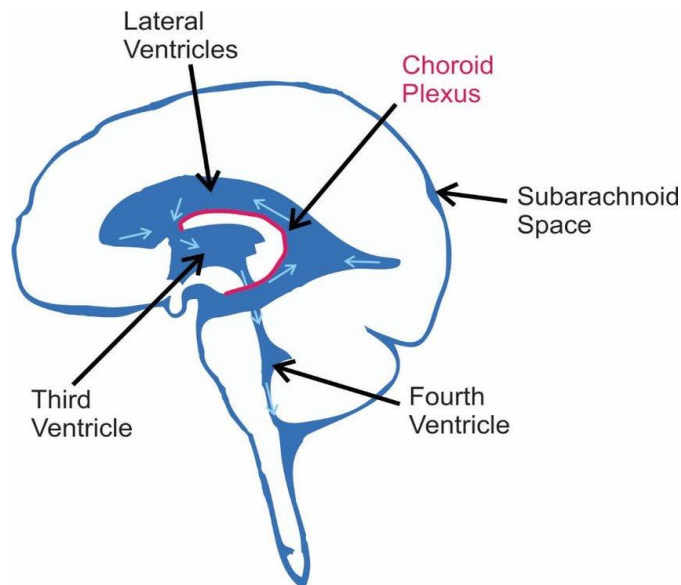
Figure 14The ventricular system in the central nervous system (27)
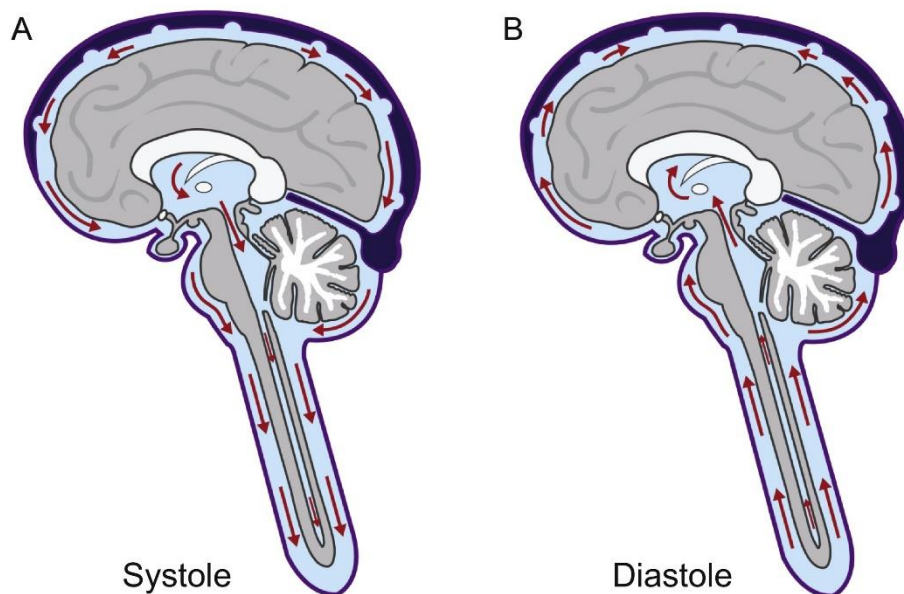
Figure 15 The flow of CSF in the Central Nervous System (A) During systole; (B) During diastole (27)

This expansion forces the CSF outflow at the foramen magnum and from there to the SAS of the spinal cord. During the diastole, the brain compresses creating negative pressure, CSF flows in a reverse direction through the aqueduct and the foramen magnum (24). In SAS, the perforated trabeculae fibers allow the flow of CSF across the SAS. Variations in CSF flow velocities have been recorded in the spinal SAS near the PAC (25). Chang et al. (26) proposed a computational model study indicating the possible role of the SAT in CSF transport and pressure in the SAS.

Blood flow in the CNS, regulated by a network of arteries and veins, influences the intracranial pressure. The arterial and venous network inside and around the skull and spinal column presents a complete vascular system with the capacity to regulate intracranial pressure. Stable intra-cranial pressure is maintained by a controlled slow release of venous blood through the inter-vertebral venous plexus. These are part of the venous drainage system of the cranium (27).

CSF cushions and supports the brain/spinal cord and it also acts as a filtration system to circulate nutrients and remove metabolic waste from the central nervous system (23).

1.2 Chiari Malformation and Syringomyelia

1.2.1 Chiari Malformation

1.2.1.1 Pathology

Neurological disorders are diseases of the central and peripheral nervous systems. CM is a neurological disorder encountered in the craniovertebral junction. CM type 1 is the most common form of this diseased condition. The pathology is characterized by descent or also called as herniation of cerebellar tonsils through the foramen magnum into the spinal compartment (Figure 16). The herniation of 3-5 mm below the foramen magnum may be considered significant in the presence of neurological signs or symptoms. The causes of this herniation into the foramen magnum are usually linked to structural defects in the brain and spinal cord, which often develop in fetal stages (28). Due to maldevelopment of the skull, the volume of the posterior cranial fossa, the space within the cranial cavity containing the brainstem and cerebellum, is essentially reduced whereas the volume of the cerebellum that sits in the space remains same. This causes herniation in the downward direction into the available space of foramen magnum (28). CM-1 can also occur in association with disorders that appear to be unrelated to skull base genetic defects such as hydrocephalus (29), intracranial mass lesions (30), CSF leaks (31), tethered cord syndrome (3) and miscellaneous conditions such as craniosynostosis (32), and Paget's disease (33).

Figure 16 Preoperative T2-weighted MRI of a patient with Chiari 1- Syringomyelia complex (37)

This compaction in the foramen magnum can disrupt the normal CSF flow along the vertebral column.

Prevalence: Based on the imaging studies, CM1 has a prevalence between 0.24% and 3.6% of the population (34). In a review of 22,591 patients undergoing brain MRI at an age-independent study, Meadows et al. (34), found that 175 patients (0.77%) with structural abnormalities such as CM-1. The frequency of diagnoses of CM-1 in the total population of 741,815 patient's underage of 20, indicating prevalence for 2 years period of symptomatic cases, was 0.7 per 10,000 (0.007%) (35)

1.2.1.2 Symptoms and treatment

Many people are asymptomatic, and symptoms mostly occur at an older age (35). The clinical findings for the CM-1 vary depending on the age of the patient. Occipital headache and neck pain are common conditions in adults. Other common symptoms such as dizziness, vertigo, hearing loss, gait abnormality are also presented (36)

Surgery is suggested based upon the severity of the diseased condition. With asymptomatic patients that have been registered with CM-1 incidentally upon MRI findings are observed and monitored with imaging studies. Patients with symptoms especially with large spinal cord syrinx(s) are recommended surgical intervention. Surgical correction may include posterior fossa decompression (PFD), with or without duraplasty. PFD includes decompressions involving only bone removal, those with incision of the outer dura layer, those opening the dura completely, and those were additional arachnoid dissection. The goal of bony decompression is to restore CSF flow at the level of the foramen magnum. Other procedures such as arachnoid dissection or shrinking of the cerebellar tonsils are also carried out. This surgical procedure is, however, invasive with a high risk of complications and the outcomes are unpredictable. A study by Faris Shweikeh et al., (37) consisting of 1593 patients with PFD surgery without duraplasty and 1,056 with PFD with duraplasty were evaluated over 10.3 years. The results of the study show, a total of 34 (1.3%) patients underwent a reoperation in the immediate postoperative period during hospitalization, 65 (2.5%) were discharged, and 387 (14.6%) experienced a complication such as hydrocephalus (5.9%), fluid and electrolyte abnormalities (2.8%) and procedure-related complications (1.4%).

1.2.2 Syringomyelia

1.2.2.1 Pathology

CM is a leading cause of syringomyelia. Syringomyelia is an elongated fluid-filled cavity within the parenchyma of the spinal cord (Figure 17). Most cases of syringomyelia are associated with CM-1 (38). In about 40-75% of the CM-1 patients, a syrinx is formed in the spinal cord (39). The syrinx causes compression of the spinal nerve fibers resulting in severe motor and sensory deficits.
Fundamentally, the volume and pressure in a cavity are determined by the inflow and outflow in the cavity. A syrinx can only expand if the inflow is greater than the outflow. Microscopically, the syrinx may be totally separate from the central canal or maybe partly lined by ependyma, which forms the epithelial lining in the nervous system. The two main indicators that may explain the syrinx formation are fluid composition and pressure. It is usually assumed that the composition of the fluid in syrinx is the same as the CSF from the spinal SAS. For the enlargement of the syrinx cavity, the pressure inside the syrinx must be higher than the SAS pressure (24).

The syrinx is more frequently encountered in the cervical region (Figure 7) of the spinal cord and can be differentiated into the following types (39):

- Type I syringomyelia is associated with obstruction of the foramen magnum with a CM-1 or another obstructive lesion, such as fibrosis or tumor.
- Type II syringomyelia is without the obstruction of the foramen magnum.
- Type III syringomyelia is associated with other diseases of the spinal cord such as spinal tumors, traumatic lesions of the cord and spinal arachnoiditis (inflammation of arachnoid mater)
- Type IV is hydromyelia usually associated with hydrocephalus. Hydromyelia is a condition which causes the dilation of the central canal and formation of ependymal lining.

Figure 17 Extensive case of syringomyelia (43)

1.2.2.2 Symptoms and treatment

K Sivaramakrishna and K Sathyavaraprasad, 2017 (40), published a study aiming to see the clinical patterns of the disease. The study was carried out with 36 patients who presented to the respective institute between October 2012 and January 2015 in whom a diagnosis of Chiari I malformation with syringomyelia was made. The studies showed the prevalence of symptoms in the following manner: 1. Neck pain in 32 patients (89%); 2. Weakness in 31 patients (86%); 3. Sensory symptoms in 26 patients (72%). As the study is limited concerning the control group, the results do not entirely explain the general prevalence of the occurrence of symptoms.

Symptoms related to syringomyelia:

- Motor
  a) Weakness and degeneration of muscle, especially in hands and arms
  b) Abnormal curvature of the spine (scoliosis)
- Sensory
  a) Reduced sensation in hands and arms.
  b) Sensation involved is also awareness of pain and temperature, or position sense.
  c) Hypersensitivity in limbs, especially in arms
- Pain
  a) Midline pain over the thoracic area
  b) Burning pain in arms
  c) Joint pain, especially in shoulders
- Autonomic symptoms
  a) Dysreflexia: wide changes in blood pressure
  b) Hyperhydrosis: plentiful upper body sweating
  c) Horner's Syndrome: Sagging of one eyelid
  d) Syncope (fainting or near-fainting)

1.2.3 Theories related to the formation of a syrinx.

The mechanism of formation of the syrinx is still unknown and numerous theories fail to explain the precise complexity of the filling of cavities. The two major challenges encountered by researchers: (1) the theories do not explain why some people develop a syrinx and others do not develop it; (2) It also fails to explain why there are rare cases of spontaneous resolution.

Some of the theories that are suggestive of the formation of the syrinx have been published but do not possess a comprehensive explanation. In a pathological study of syringomyelia by Milhorat et al. (3), three types of syrinx were identified, as shown in Figure 18: (1) dilations of central canal in connections to the fourth ventricle;(2) dilations of central canal isolated from the fourth ventricle; (3) extra canicular cavitation in the parenchyma that does not involve the central canal. Several theories have been proposed to explain the mechanism causing syrinx formation. Though the study does not imply the actual mechanism, the role of CSF hydrodynamics and pressure propagation have received attention.
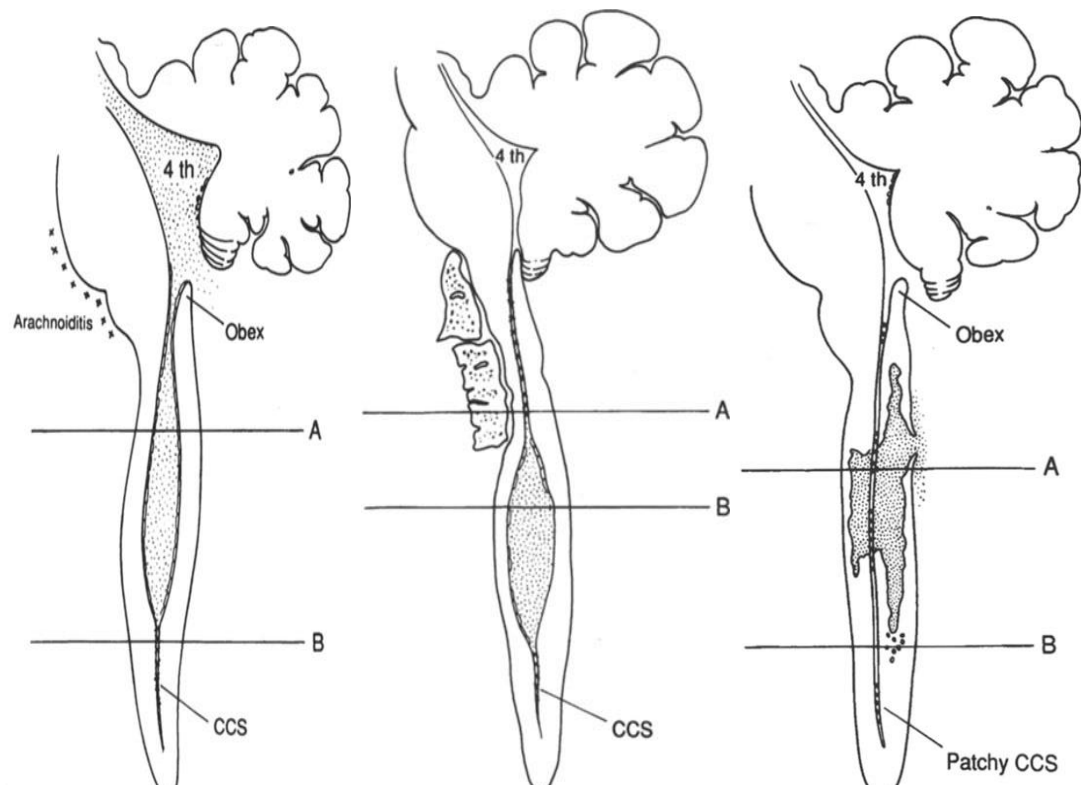
Figure 18 (a) Communicating syringomyelia; (b) Noncommunicating syringomyelia; (c) Posttraumatic syringomyelia without any interaction with the central canal (3). CCS: central canal stenosis

A theory proposed by Koyanagi, et al. (41) states that abnormal and increased pulsatile motion of the cerebellar tonsils can produce an impaired flow of CSF during the systole as the pressure is high during this phase of the cardiac cycle. This abnormality is transmitted to the spinal SAS and drive the CSF into the central canal of the spinal cord. through perivascular and interstitial spaces that lead to syrinx formation (36). Another theory put forth by Oldfield et al. (42) and Heiss et al. (43), suggests that the cerebellar tonsils are displaced up and down during the cardiac cycle, thereby creating a piston effect on the spinal SAS which is partially blocked. This leads to flow from the SAS directing into the spinal cord tissue and causes pulsatile syrinx flow, leading to syrinx

formation. A disturbance of the CSF flow across the spinal cord due to constricted SAS is a common component for building up the hypothesis ((4); (28); (44)). Syringomyelia cavities associated with CM are often found in the cervical spinal cord region, presumably where the pressure disturbances are more prominent. However, newer evidence shows that the severity of CM tonsil protrusion does not always correlate with syringomyelia cavity development (41) and that other factors such as insufficient space in the lower skull (posterior fossa) or the shape of the cervical spinal canal((45); (46)) can play an important role. This may explain the lack of pressure dissociation observed in some patients with CM and syringomyelia. That, however, would imply an alternate theory to pressure dissociation is responsible for causing syringomyelia in these cases. Another hypothesis was put forth suggesting that in CM patients, the syrinx communicated freely with the fourth ventricle and that its enlargement was rooted in altered stresses in the hindbrain region. It has since been determined that the syrinx cavity often does not communicate freely with the fourth ventricle (47).

1.2.4 Treatments:

Post-traumatic and Post-inflammatory Syringomyelia
The treatment for the syringomyelia is the placement of shunt into the cavity to divert the fluid into the abdominal cavity or the chest cavity. This procedure is a common treatment for syrinx formed due to trauma or spinal injury. Due to the low success rate of re-operation due to shunting, the procedure is abandoned by many surgeons (48). Shunting failure rates of up to 50% have been recorded for syringomyelia following SCI (24). A shunt treats the cavity but not the underlying cause and as such is used when other methods have failed or if it carries a lower risk than other options. Whether a shunt is used to treat a syrinx caused by SCI or CM, several studies have noted that the SAS blockage must be removed for a truly beneficial outcome (Figure 19)((24); (49)) highlighting the common hypothesis that disturbed CSF ow is a key factor in syrinx formation.
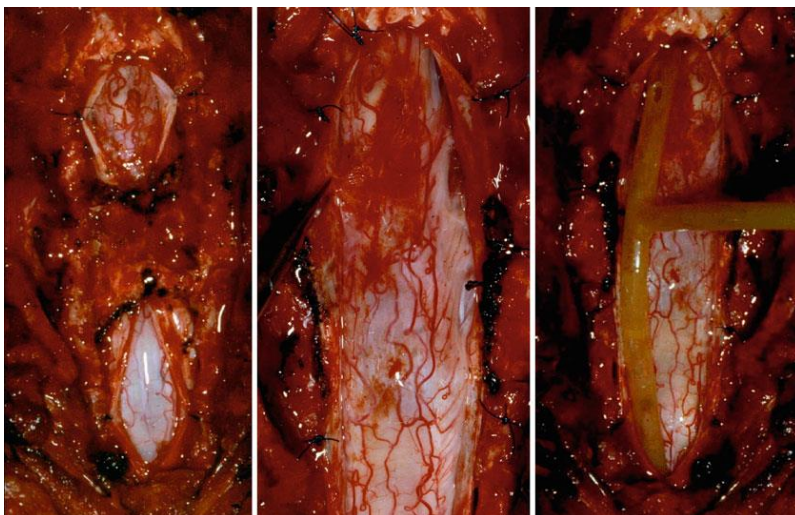
Figure 19 Step-by-step shunting process to drain the fluid from the syrinx (31)

CM-1 related Syringomyelia

As the CM is the precursor for this certain condition, surgeons operate on the cause of it. In cases of syringomyelia due to CM, the spinal cord is untethered through laminectomy (removal of the dorsal part of the spinal column) and posterior fossa decompression (PFD). This surgery can allow the syrinx to drain, sometimes becoming smaller or even disappearing entirely (Figure 20). Symptoms may improve even if the syrinx remains the same size or is reduced only slightly (49).
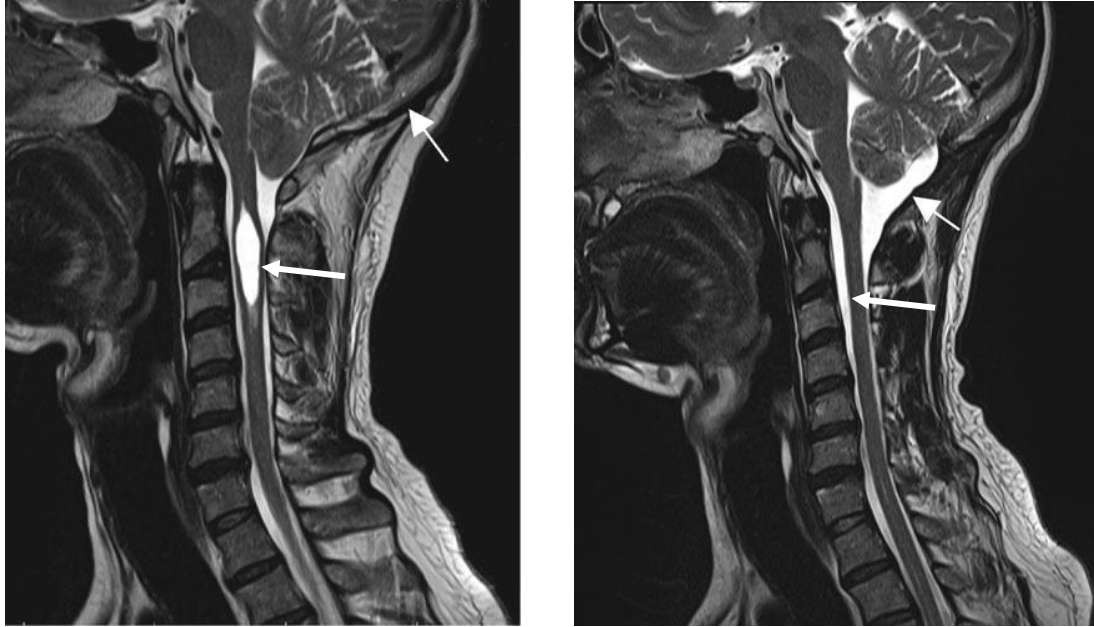
Figure 20 (a) Preoperative T2 weighted MRI scan of CM-1 and associated syrinx; (b) Postoperative T2 weighted MRI scan with posterior fossa decompression surgery and resolution of the syrinx (53)

1.3 State of the art

Neurosurgeons regularly make judgments involving the mechanical properties of the spinal cord and brain. The diagnosis and treatment are based upon the findings on the mechanical properties such as pressure acting on the hindbrain due to the herniation of tonsils in the case of CM-1 and the consequent deformation of the tissue. During the surgery, the surgeons may gently palpate the exposed tissue to estimate the compliance and degree of the diseased condition, for example, the location and size of the syrinx in the spinal cord. There is uncertainty in surgical intervention for syringomyelia and difficulties in carrying out experimental work such as monitoring a patient with the severe diseased condition is tedious and invasive for the patient. This makes mathematical modeling of the biological tissue and their mechanics of this condition a very feasible tool for research.

CM-1 in humans is like a condition called Chiari-like malformation that is common in several toy breed dogs including two genetically related dog breeds. The dog model is the only known naturally occurring animal model for Chiari type I malformation and syringomyelia. A study by Karlsson and Lindblad-Toh, 2008, (50) showed that purebred dogs represent an invaluable tool for mapping and cloning genes, proteins, and molecular pathways involved in normal and abnormal development of structures of the human craniovertebral junction.

Besides these vivo models, syringomyelia models have been developed using a variety of different methods. These range from physical models using materials with comparable properties to biological tissues, computational and mathematical models of the whole spinal cord, and related fluid system. Below are some of the syringomyelia modeling techniques, underlining the need for more detailed models of the spinal cord tissue and extracellular fluid when analyzing hypotheses of syrinx formation.

1.3.1 Mathematical Modelling approach

1.3.1.1 Computational Fluid Dynamic models

The connection between disturbed CSF flow and syringomyelia is well proven (28), yet the exact mechanisms involved are still unknown. Numerous computational fluid dynamics (CFD) models of fluid in the SAS have been used to examine how CSF pressure and velocity are affected by CM-1 and spinal cord traumatic injury. This study shows the effect of disturbed CSF on the cord tissue. A two-dimensional model of the spinal cord and surrounding fluid (51), demonstrated that the presence of a modeled central canal does not change the CSF movement but increases radial pressure gradients within the spinal cord. The condition used here was an oscillatory fluid flow in the with and without the presence of a central canal in the spinal cord.

Clarke et al. (52) developed three subjects specific CFD models for a normal patient, a CM with syringomyelia, and a CM without syringomyelia (Figure 21). The conditions for the simulations were velocity measurement from MRI images from the respective cases.

They found that CM produces higher SAS pressure in a computational fluid dynamics (CFD) model. When a syrinx was introduced to the CM model, pressures in the SAS were like a healthy SAS model. The results were in good congruence with the results that have been noted in other studies ((4); (53)).
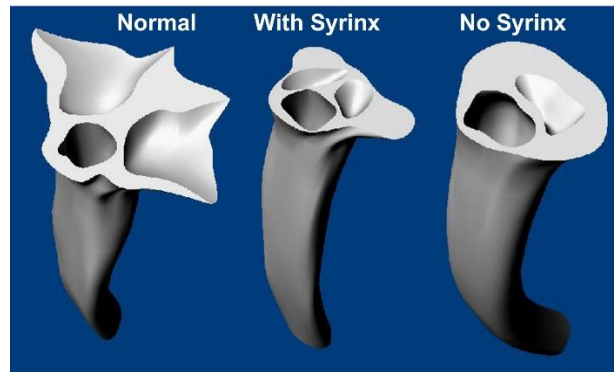
Figure 21 The CSF volumes for the 3 cases from the inlet side (51)

Another study by Sumeet Gupta et al. (54), aiming at investigating three-dimensional subject-specific CSF dynamics. The group used a combination of finite-volume analysis and computational fluid dynamics and MRI experiments. Creating a 3 D patient-specific reconstructed model involving the trabecula network in the spinal SAS, as shown in Figure 23, and using the data obtained from Velocimetric MRI (used to measure the velocity field at these boundaries) (Figure 22). The findings were that the net volumetric flow rate in the spinal canal was negligible despite CSF oscillation with significant amplitude.
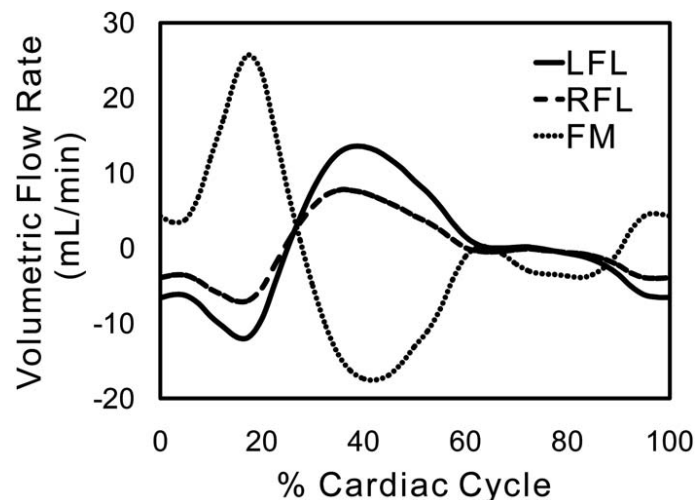
Figure 22 CSF volumetric flow rates based on cardiac cycle used as inlet condition at Left foramen of Luschka (LFL), Right foramen of Luschka (RFL), Foramen of Magendie (FM) (53)
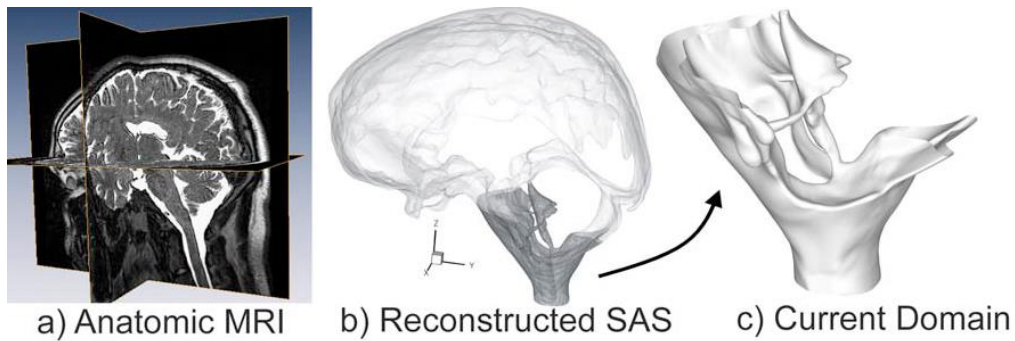
Figure 23 3D reconstruction of the SAS using anatomic MRI (53)

This syrinx related SAS pressure decline further supports the link between syringomyelia and CSF disturbance. Moreover, it suggests that in the presence of abnormal CSF movement, the spinal cord tissue cannot endure the stresses it is subjected to and a syrinx may form as a kind of compensation for the disturbed SAS pressure.

The CFD models provide useful insight into CSF dynamics and wave propagation in the spinal cord (4), however, an investigation of internal tissue behavior is required to comprehend the mechanisms underlying syrinx formation. Linge et al. (55), demonstrated a patient-specific model to compute the effect of craniovertebral decompression on CSF pressures and velocities in the posterior fossa, foramen magnum, and cervical spinal canal (Figure 24). An asymmetrical sinusoidal waveform was applied, with the upward flow (diastole) lasting twice as long as the downward flow (systole) and having half the amplitude as an inlet at the cranial end of the model. This CFD study showed a decrease in CSF velocities similar to those found in studies in which PC MRI was used (55).
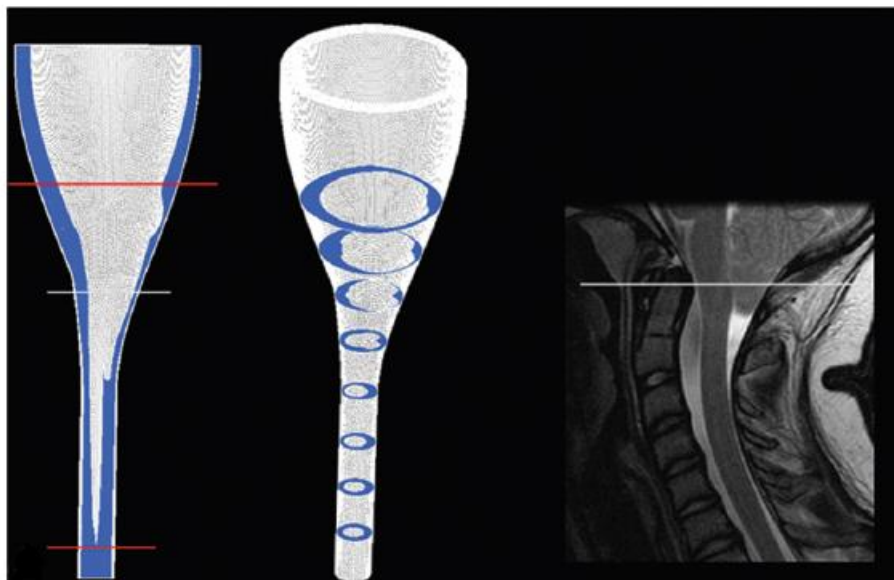
Figure 24. The computational model is shown with sagittal MR images showing a typical Chiari I malformation (54)

A recent CFD study by Martin et al, 2019 (56), patient-specific modeling of the CSF including nerves, blood vessels, and trabeculae (Figure 25). The boundary conditions used were drawn from combined CSF production rates in the choroid plexus of the third

and lateral ventricles. The integration of an MRI-acquired CSF flow profile in the aqueduct of Sylvius over a cardiac cycle was used. The results from the simulation showed that the inclusion of nerves, blood vessels, and trabecular microstructure had relatively little impact on the CSF velocity profiles but did influence local flow mixing to a great degree.
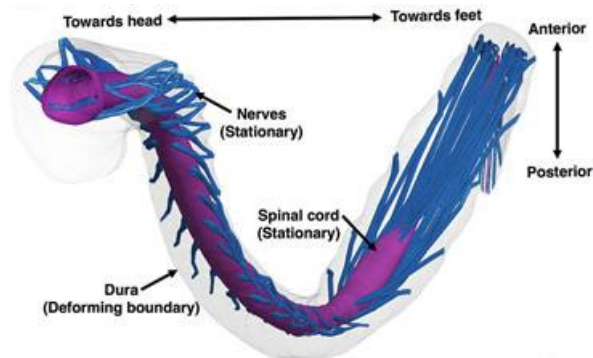
Figure 25 The geometric domain used for the spinal CFD model based on a freely downloadable spinal SAS (55)

1.3.1.2 Physical models

Physical models of the spinal cord and SAS are relatively uncommon (57); (47). They allow pressure measurements within the cord and SAS to be taken while complying with physical conditions that would be otherwise simplified or neglected in computational models. Physical conditions such as elastic properties of the spinal cord and CSF waveform for the fluid flow, as shown in Figure 27., are used for modeling. The pressure measurements are taken from in vivo in patients and animal models. The main challenge the researcher's face is finding materials that comply with the biological tissues, however physical models provide useful data to validate the results from computational and in vivo models. Martin and Loth (2009), (57) measured pressure in and around the spinal cord following a simulated cough (Figure 26). The results showed that the presence of a syrinx and a SAS blockage increased the pressure gradient in the SAS. It contradicts the findings from CFD studies that showed reduced pressure gradients in the presence of a syrinx. However, this could have been a result of the selected elastic polymer material used to represent the cord, as it was much stiffer than spinal cord tissue is thought to be (500 kPa as opposed to 5 kPa). After demonstrating the cough pulse, it was recorded that the pressure in the SAS was relieved by the presence of a syrinx.
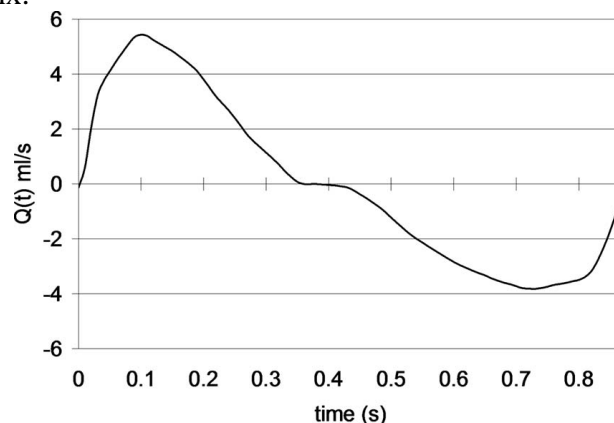
Figure 26 The cyclic CSF flow waveform as input (56)
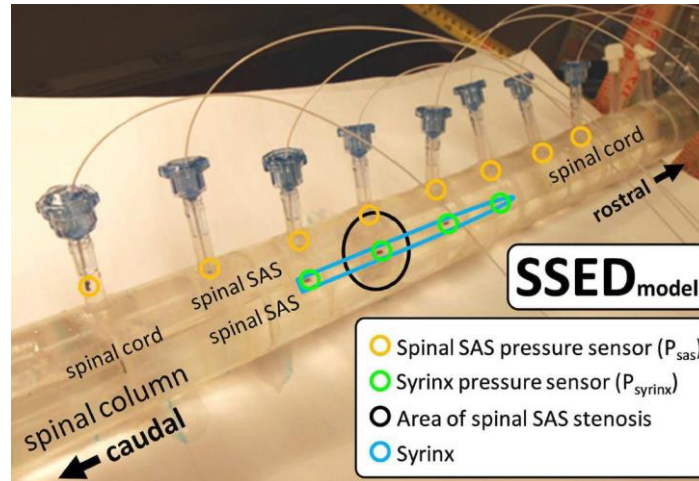
Figure 27 Physical model representing the spinal cord with a syrinx, inside a flexible spinal column containing a partial (90%) blockage (referred to in the image as stenosis). The pressure is measured via the catheters along the top (56)

1.3.1.3 Fluid-structure interaction models

The previous sections have described models that have focused either on the CSF movement or the mechanical behavior of the CNS. A new set of models concentrates on stresses and pressures within the spinal cord parenchyma tissue itself when the cord is subjected to CSF pressures that have been disrupted by injuries and conditions such as CM-1 that led to syringomyelia. More recent fluid-structure interaction (FSI) models use a combination of CFD with spinal cord tissue as a linearly elastic material (structural mechanics) model. These are computational models using finite element or other numerical methods to calculate stress in the cord. The cord is often modeled as a linear or viscoelastic material, although poroelastic models that include the extracellular fluid component of tissue and effect of perivascular spaces provide deeper knowledge into the effect of tissue type on the described condition.

Bertram 2010 (58), designed a model of the cord as a viscoelastic material subjected to loading such as excitation due to coughing and revealed that tensile radial stresses were insufficient to damage the tissue. However, when the cord is subjected to constant small stresses as a result of breathing, pulse, or movement combined with SAS blockage, this could have a collective effect. Poroelasticity has long been used to represent many biological tissues such as bone, heart, cartilage, brain, and spinal cord ((59); (60); (53)) as it registers the behavior of both the solid and fluid parts of these tissues. It is thought to provide a reasonable representation of biological material behavior (61).

An axisymmetric poroelastic model of the spinal cord by Harris and Hardwidge, (60), found higher stresses near an existing cavity, implying that once a cavity is formed it is likely to worsen (Figure 28).
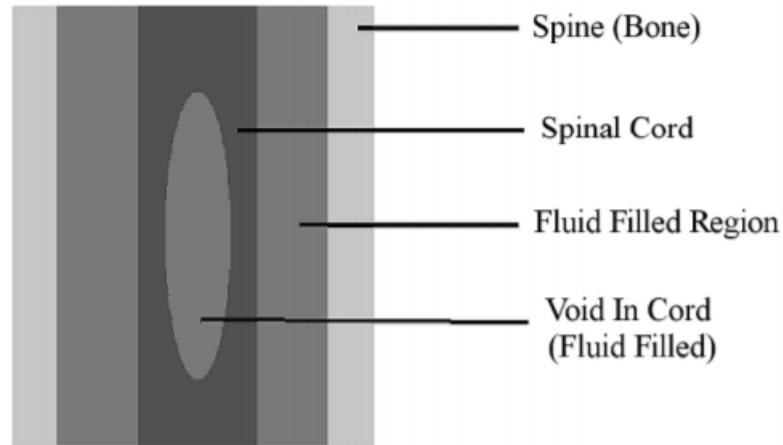
Figure 28 Axis-symmetric porous model with a void in cord displaying syrinx (60)

CFD models have included a poroelastic spinal cord by Støverud et al. (53), to evaluate the effects of CSF flow and determine whether internal tissue stress could be high enough to damage the cord. Modifying the tissue properties and anatomical structures, 11 variations of the model were created to compare the results of varying tissue properties (Figure 30). The results show that an open segment of the central canal and stiff pia both increase the radial pressure gradients and induce interstitial fluid flow in the central canal.
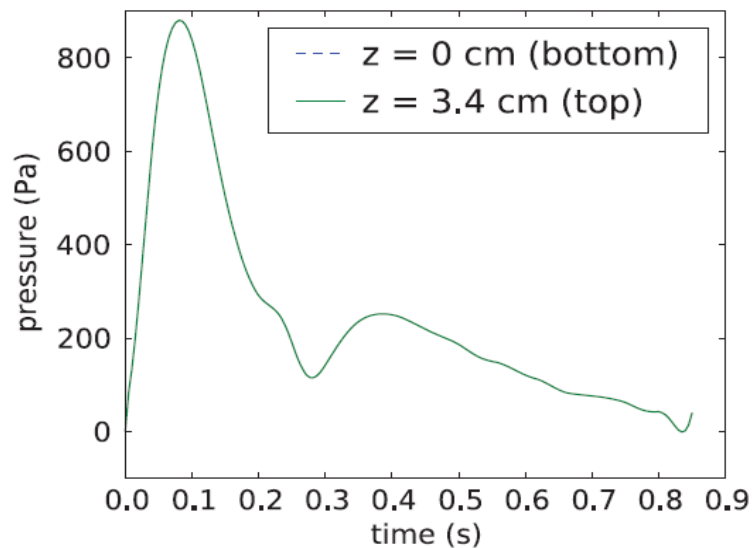
Figure 29 The pressure wave based on in vivo intracranial pressure measurement in CM-1 patient used as an inlet boundary condition (52)
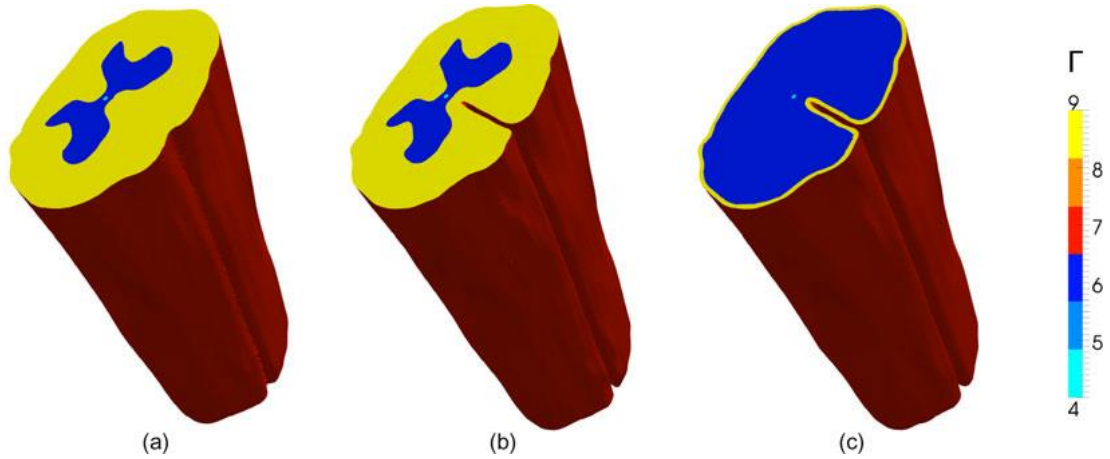
Figure 30 Representation of some geometries of the spinal cord reconstructed from MRI images of sheep cadaver and used in the simulations (52)

The FSI of a two-dimensional axis-symmetric model of the spinal cord by Bertram C. D, 2010 (58), was developed to study the effects of spinal subarachnoid- space stenosis on the adjacent syrinx. The simulations were carried with a pressure pulse excitation applied at the cranial end of spinal SAS (Figure 31). The findings where a bulk fluid flow beyond the stenosis gave rise to pressure dissociation in the longitudinal direction in the spinal SAS adjacent to the syrinx. These models have calculated increased pressure gradients above and below a partial obstruction of the SAS. An upgrade to the already existing 2D axisymmetric model, Bertram, and Heil, 2017 (59), included poroelasticity to the spinal cord tissue while keeping the dura mater as linearly elastic similar to the previous model. The results obtained varied slightly with the previous model. There was slight oscillatory shunt flow bypassing the stenosis via porous tissue. It demonstrated the possibility of increase of syrinx volume when the cord and pia mater is permeable.
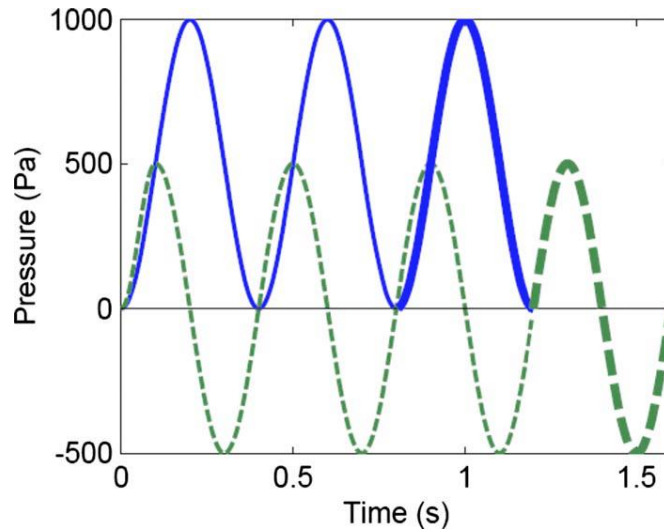
Figure 31 The two waveforms of periodic excitation applied to the cranial end of the fluid model (58)

2. Methods

To numerically simulate the behavior of the spinal cord under the physical conditions, a mathematical model that describes its physiological behavior must be derived. As it is established that poroelasticity provides a more realistic representation of biological tissues (61). In this study, the theory of poroelasticity is used to model the spinal cord tissue, while the fluid flow in the spinal SAS is given by Darcy's velocity. Modeling poroelasticity combines two physical laws namely, Darcy's law and the structural mechanics. Darcy's law describes the relationship between fluid motion and pressure in the porous media. The structural mechanics describes the effect of the fluid motion on the porous media.

2.1 Theory of poroelasticity

The theory of poroelasticity put forth by Biot describes the mechanism of squeezing fluid from an elastic porous media. The theory states that a porous media can be treated as an elastic material that is governed by Hooke's law and the fluid flow through the pores is governed by Darcy's law ((62); (63); (64)). Darcy's law along with the continuity equation and the equation of state for the pore fluid provides a complete mathematical model of elastic porous media. As the fluid loses considerable energy due to friction resistance in the pore matrix, the flow velocities in porous media are very low. Darcy's law states that the velocity field is determined by the pressure gradient, the fluid viscosity, and the structure of the porous medium. According to Darcy's law, the net flux across the face of a porous surface is.

$$\boldsymbol{u} = -\frac{\kappa}{\mu}(\nabla p + \rho g \nabla D) \text{ (Equation 1)}$$

In this equation, u is the Darcy velocity (SI unit: m/s); κ is the permeability of the porous medium (SI unit: m^2); μ is the fluid's dynamic viscosity (SI unit: Pa·s); p is the fluid's pressure (SI unit: Pa) and ρ is its density (SI unit: kg/m^3); g is the magnitude of gravitational acceleration (SI unit: m/s^2); and ∇D is a unit vector in the direction over which the gravity acts. Here the permeability, κ, represents the resistance to flow over a representative volume consisting of many solid grains and pores.
The Darcy's law interface combines Darcy's law with continuity equation,

$$\frac{\partial}{\partial t}(\rho \varepsilon) + \nabla.(\rho \boldsymbol{u}) = Qm \text{ (Equation 2)}$$

In the above equation, ρ is the fluid density (SI unit: kg/m^3), ε is the porosity, and $\mathbf{Q}_m$ is a mass source term (SI unit: $kg/(m^3 \cdot s)$). Porosity is defined as the fraction of the control volume that is occupied by pores.
Inserting Darcy's law (Equation 1) into the continuity equation produces the generalized governing equation:

$$\frac{\partial}{\partial t}(\rho \varepsilon) + \nabla.\rho\left[-\frac{\kappa}{\mu}(\nabla p + \rho g \nabla D)\right] = Q_m \text{ (Equation 3)}$$

2. Methods

Porous Matric Deformation:
The poroelastic material model uses the following equation to describe changes in the stress tensor σ and porous matrix displacement u and changes in pore pressure:

$$-\nabla.\sigma = \rho\boldsymbol{g} \quad \text{(Equation 4)}$$

here, σ is the stress tensor, ρ is the total density, and g is the acceleration of gravity. the time rate of change in strain $d\varepsilon_{vol}/dt$ appears as a coupling term in Darcy's Law and Solid mechanics. For an isotropic porous material under plane strain conditions, this simplifies to

$$\begin{bmatrix} \sigma_{xx} \\ \sigma_{yy} \\ \sigma_{xy} \end{bmatrix} = \frac{E}{(1+v)(1-2v)} \begin{bmatrix} 1-v & v & 0 \\ v & 1-v & 0 \\ 0 & 0 & 1-2v \end{bmatrix} \begin{bmatrix} \varepsilon_{xx} \\ \varepsilon_{yy} \\ \varepsilon_{xy} \end{bmatrix} - \begin{bmatrix} \alpha_{B}p & 0 & 0 \\ 0 & \alpha_{B}p & 0 \\ 0 & 0 & \alpha_{B}p \end{bmatrix}$$

(Equation 5)

where E is Young's modulus (Pa) and σ is Poisson's ratio of the drained porous matrix. The term $\alpha_{B}p$ (Pa) amounts to the fluid pressure contribution and is often described as the fluid-to-structure coupling expression.

2.2 Model specifications

The study aims to design a two-dimensional axis-symmetric model of the spinal and carry out simulations with poroelastic spinal cord tissue. The model is a two-dimensional axis-symmetrical geometry designed in a commercial finite-element software COMSOL-Multiphysics® 5.5, COMSOL Inc., Proprietary EULA. It consists of two physics fluid mechanics and structural mechanics, combined by poroelastic coupling.

The geometry of the model is derived from the anatomical details of Crossman and Neary, 2018; (5), and Bertram C.D., 2010; (58).

The model is a long cylindrical tube that tapers inwards at the end (from cranial to caudal direction), with a total length of 600 mm. It consists of four axisymmetric layers of the spinal cord tissue, the spinal meninges and filum terminale. The first layer, from the axis of symmetry (represented in red in Figure 32)in the radial direction, is the spinal cord tissue. It has a diameter of 11.6 mm. It also has a syrinx in the cervical region with a 20% cavitation concerning the diameter of the spinal cord. As the model tapers, the syrinx cavity also tapers slightly inwards with conical ends of approximately ~23°. The spinal cord tissue is uniform till the sacral region, it becomes dense concerning the material properties as it tapers into ultra-thin filum at the extremity. To increase the caudal damping of pressure wave propagation, filum is included in the model (58). Adjacent to the spinal cord is a fine layer of pia mater of thickness 0.2 mm. The pia mater is continuous with identical thickness up to the extremity. The third layer is fluid-filled spinal SAS, of thickness 4mm. The thickness varies over the length of the model. The geometry is adapted based on a computer tomography study (Figure 33) (58). The last layer is the dura mater with a uniform thickness of 1mm throughout.

2. Methods
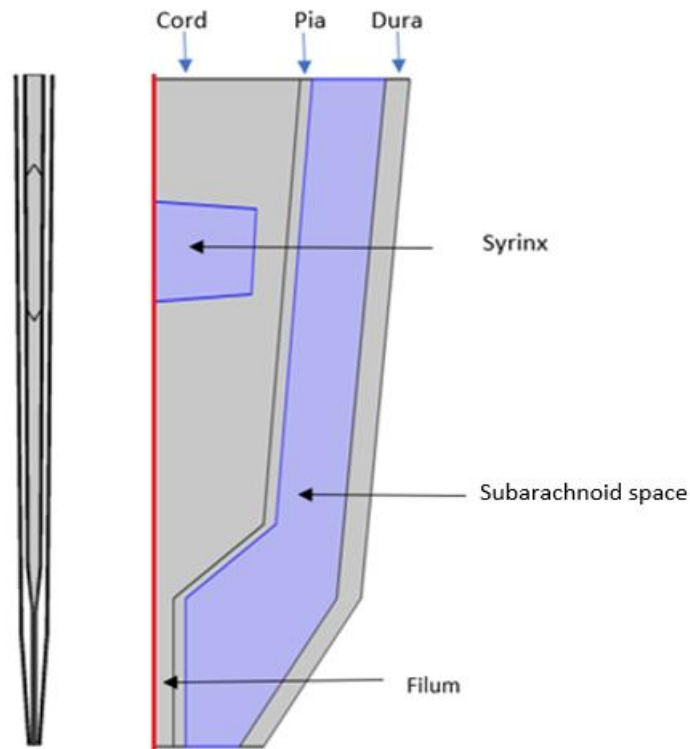
Figure 32 Two-dimensional axisymmetric spinal cord model and the radial dimensions scaled up 20× relative to the axial distance.
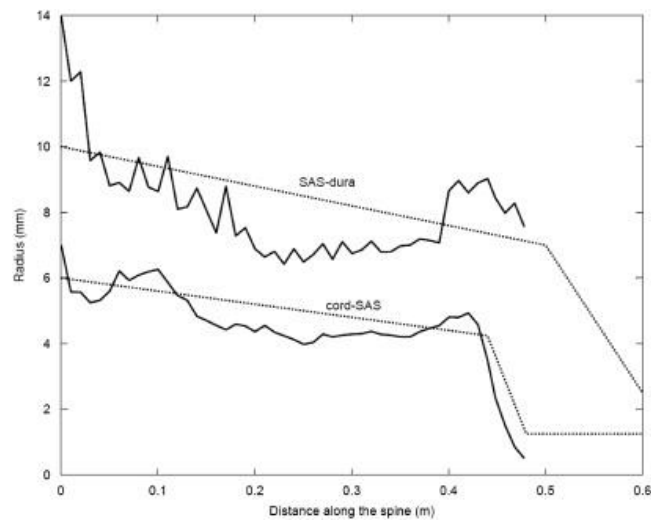
Figure 33 Comparison of dimensions of modeled SAS with data from computer tomography of cord and dura, SAS (63)

2.3 Material properties

For different phenomena or physics to be simulated, different sets of material properties are required.

1. Fluid: The CSF in the spinal SAS and syrinx is given the material properties similar to water which are as follows:

2. Methods

Table 1. Properties of fluid

Fluid-filled compartments	Syrinx and SAS
Viscosity at 37° C	7e-4 [Pa*s]
Density	1000 [kg/m^3]
Bulk modulus	2.1 GPa

2. Elastic material: Young's modulus and Poisson ratio are required for the stress analysis of solids and structures. The mechanical properties of the tissues comprising the cord, pia filum, and dura were based on the values proposed by Bertram et al.; (59). The cord, pia, and filum are considered to be linearly poroelastic. The differentiation between the material properties of grey and white matter of the spinal cord parenchyma is considered negligible in this study. The properties of linear poroelastic material are defined by a set of parameters such as Young's modulus, Poisson's ratio, permeability, and porosity. Parameters such as permeability and porosity are equal for the cord, pia, and filum. The values of porosity and permeability are derived from an experiment carried out by Hui Zhang et al. (65), Neurite Orientation Dispersion and Density Imaging (NODDI), a practical diffusion-weighted MRI technique is used to estimate the microstructural complexity of dendrites and axons in vivo on clinical MRI scanners. The technique uses modification to the MRI measurements according to the displacement pattern of water molecules undergoing diffusion in spaces formed by the microstructural environment (66). Porosity is considered to be a fraction of spinal cord tissue not occupied by the axons of neurons. Permeability in the spinal cord is the ease with which the extracellular fluid can move through the extracellular and perivascular spaces when the pressure gradient is applied. The values of Young's Modulus and Poisson's ratio is different for different tissue type depending on the type of testing technique used and physical conditions implied on the tissue during the test in vivo. A study by Gupta et al. (54), suggested the presence of a trabecular network in the SAS complicates the investigation of the flow field. To make the model realistic concerning the composition and material properties, the trabeculae network is added to the SAS with material properties assigned as shown in Table 2. The values of the material properties are derived from an experiment carried out by Mortazavi et al. (16). The dura mater is linearly elastic material for this study with considerably higher Young's Modulus than the spinal cord tissue. The values for the poroelastic material are tabulated as follows:

Table 2. Properties of Linear poroelastic material

Parameters	Porosity	Permeability	Source
Cord	0.2	1.4e-14[m^2]	Zhang et al. (2012) (65)
Filum	0.2	1.4e-14[m^2]	Zhang et al. (2012) (65)
Pia	0.2	1.4e-14[m^2]	Zhang et al. (2012) (65)
SAS	0.99	8e-7[m^2]	Gupta et al. (2009) (54)

2. Methods

Table 3. Properties of Linear poroelastic material

Parameters	Young's modulus [MPa]	Poisson ratio	Source
Cord	0.005	0.35	Bertram (2017) (59)
Filum	0.0625	0.35	Bertram (2017) (59)
Pia	1.25	0.35	Bertram (2017) (59)
SAS	0.001	0.48	Mortazavi et al. (2017) (16)

Table 4. Properties of Linear elastic material

Solid material	Young's modulus [MPa]	Poisson ratio	Source
Dura	1.25	0.49	Bertram (2017) (59)

2.4 Boundary Conditions and Initial values

Boundary, initial, and loading conditions play a decisive role in the simulation. Boundary conditions in the Poroelasticity module are fully coupled using the Biot-Willis coefficient equals 1. This states the time rate of expansion of the porous matrix. An inlet pressure condition at the entry of the SAS was imposed (Figure 34 (a)). The system was transiently excited by a pressure wave. The characteristics of the pressure wave forcing the fluid into the SAS were derived from a study by B Williams, (67).In this study, 32 subjects of conscious seated normal patients reported a mean pulsation of 4.29 mmHg in the ventricles and 4.11 mmHg in the lumbar area. Based on these recordings, a sine wave of the amplitude approximately equal to 500 Pa with frequency 1.25 Hz corresponding to the cardiac cycle is imposed at the cranial end of the spinal SAS (Figure 35). It mimics the bidirectional flow of the CSF in the SAS. The frequency is chosen in such a way that a cycle of systole following diastole is completed in a total of 0.8s corresponding to the arterial pulse. Another pressure pulse of amplitude approximately equal to 700 Pa is used when the effect of the fourth ventricle on the flow dynamics is considered later in the simulation.

2. Methods

a   b
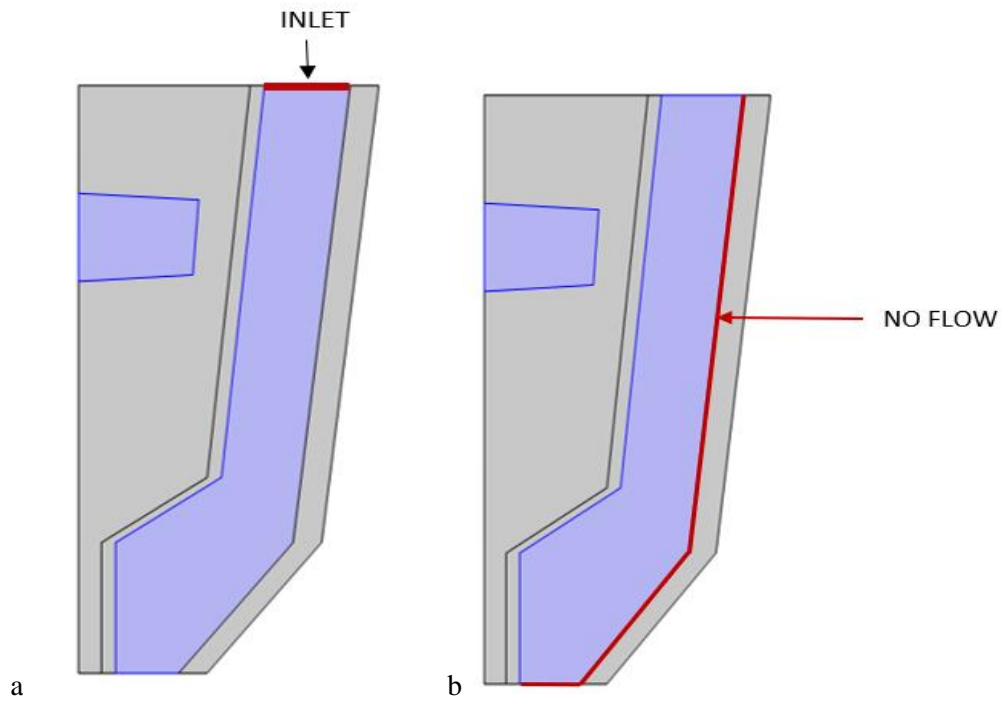
Figure 34 (a)Inlet condition at the cranial end of the spinal cord; (b) No flow condition at the wall
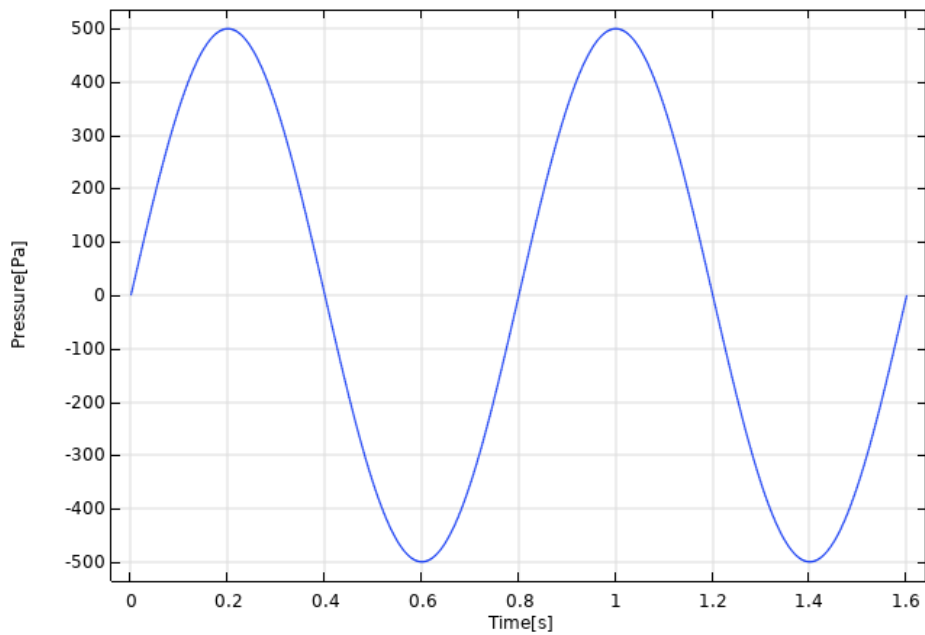
Figure 35 The waveform of periodic excitation is applied at the cranial end of the fluid model.

The wall with no flow condition is described in Figure 34 (b). The condition is automatically updated by the coupling of physics in COMSOL-Multiphysics® software. The highlighted portion with a red dotted line depicts the axis of symmetry. It is assigned in such a way that the syrinx fluid could not cross the axis of symmetry. To avoid the axial motion of the solids, a fixed constraint, as shown in black in Figure 36, is imposed on the cranial and caudal edges of the spinal cord tissue. With the open end of the dura mater depicted as a free wall in the simulation (Figure 32). With initial

conditions such as displacement field and structural velocity field are set to zero, for the solid mechanics' node. For fluid flow-node, the initial conditions of pressure are set to zero.
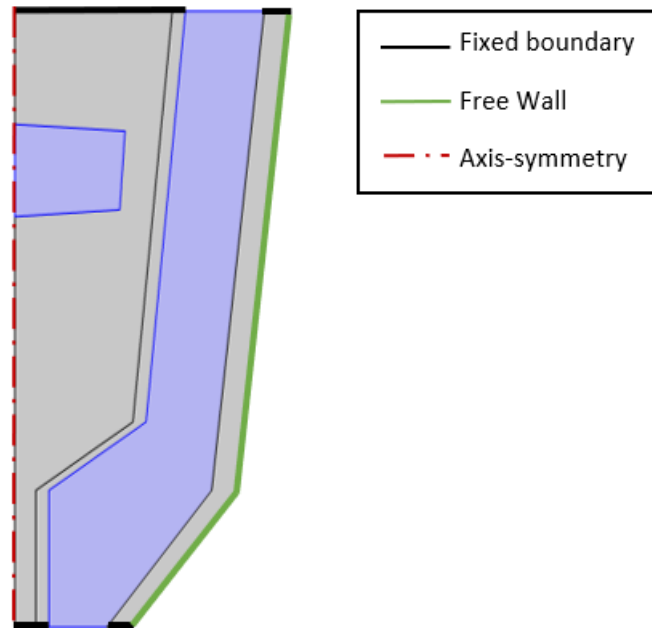
Figure 36 Initial conditions for the coupling of physics

The simulation was carried out in two steps: a) Stationary study and b) time-dependent study. The stationary study was carried out to establish initial values of unknown parameters, such as displacement, stress, and velocity of the fluid. It was also a crucial step in carrying out the mesh sensitivity study. While the time-dependent study was carried out for two cardiac cycles as an inlet condition. It took 10 hours to complete the simulation with time stepping of 0.02s using default time-dependent nonlinear solver. As time-stepping plays a decisive role in describing the pressure and velocity fields in the model, it was chosen such that solutions at every step can be visualized efficiently without any additional computational costs. The convergence was achieved by overcoming relative tolerance of 0.01 and absolute tolerance of 10^{-3} with the number of iterations equal to 200.

2.5 Surface Mesh and Mesh Sensitivity Study

A physics-controlled surface mesh was generated to accommodate the spinal cord geometry. The Free Triangular meshing is a quick and simple way to obtain meshes of high element quality that cover the whole geometry. Although the unstructured mesh generated using this method has a drawback of more numerical diffusion than the structured mesh. Using an adaptive mesh provides a more stable numerical solution as the mesh adjusts to the solution at every iteration. A mesh refinement study was carried out to make the solutions independent of the mesh densities and to limit the computational time. The skewness is a suitable measure for most types of meshes. This quality measure is also used when reporting bad element quality during mesh generation. The density of mesh selected for transient simulation was based upon the skewness of the mesh.

Triangular elements were used for the spinal cord, pia mater, SAS, dura mater, and filum. The quality of mesh elements varied to every part of geometry depending upon the dimensions. As the pia mater is ultra-thin, fine elements were generated at the section. The minimum element quality of 0.3 skewness was set for every mesh element using the element order method of the refinement technique. In this technique, the element order is changed based upon the refinement steps at every level without the need for remeshing. Two refinement levels were used in this particular study.

The following physics-controlled mesh densities were generated:

Table 5. Different mesh densities for mesh sensitivity analysis

Mesh Number	Total Number of elements	Degree of freedom
1	155695	12,10,030
2	177317	14,73,689
3	195890	17,41,973
4	201971	25,06,122
5	318411	32,17,014

Studying convergence required choosing an appropriate mesh refinement metric to get a good approximation of results. The global metrics chosen for the mesh sensitivity study were as follows.

1. Darcy's Velocity (m/s)
2. von Mises stress (N/m2)
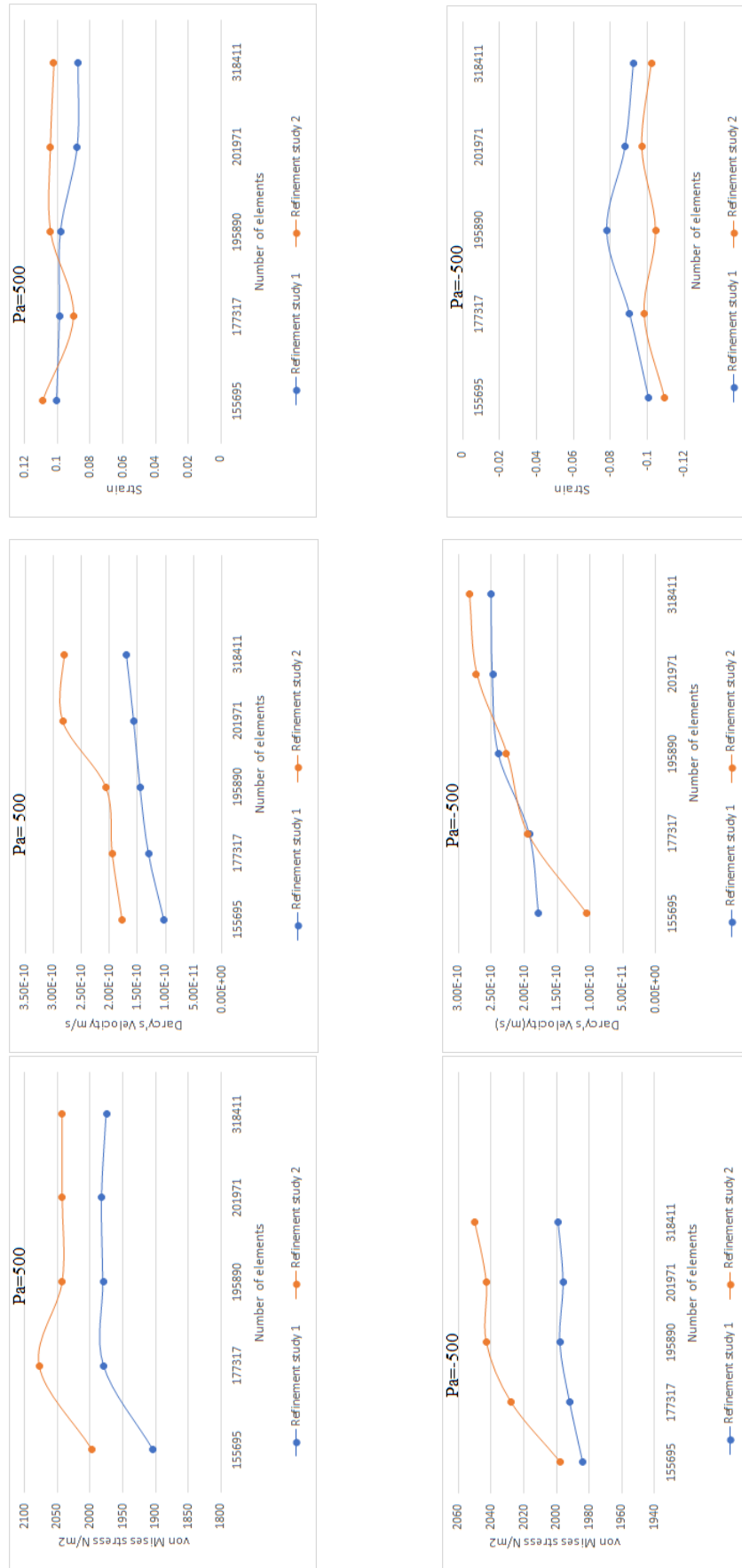3. Strain

2. Methods

Figure 37 The plots of von Mises stress, Darcy's Velocity, strain versus the mesh densities. The results were obtained from a stationary study for two different pressure conditions i.e., 500 Pa and -500 Pa.

52

The most efficient mesh was chosen when the graph of a given metric converged at the last points at each pressure condition. This depicts the convergence was nearly reached. The convergence was achieved by overcoming the relative tolerance of 0.01 and absolute tolerance of 10^{-3}. For both the refinement levels, the convergence was reached at mesh densities with 201971 and 318411. Due to the refinement process, the minimum element quality for the 201971-mesh density was reduced to 0.27. To reduce error due to minimum element quality, mesh density of 318411 was selected. The characteristics of the chosen mesh density are as follows.

Table 6. Characteristics of the chosen mesh

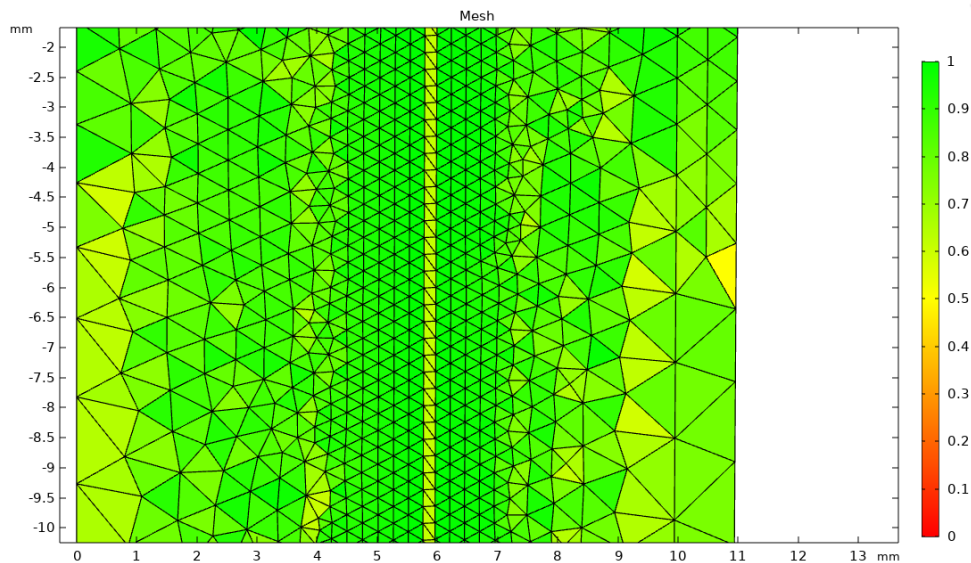|	
Total Number of elements	**318411**
Minimum element quality (skewness)	**0.3298**
Average element quality(skewness)	**0.8382**
Element area ratio	**6.666E-4**
Total number of free triangular elements	**257644**

Figure 38 Skewness of the chosen mesh
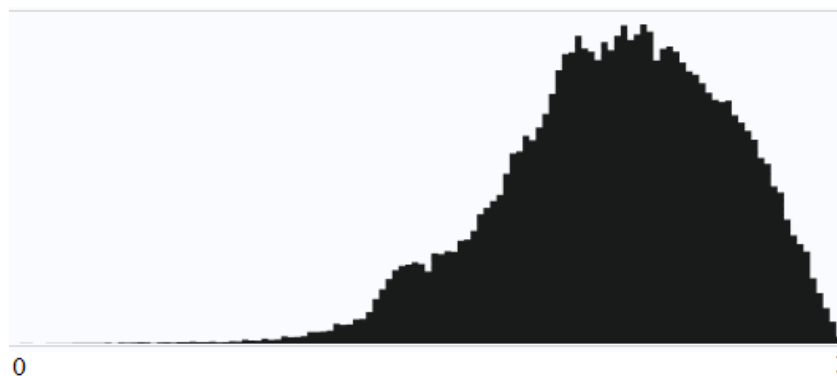
Figure 39 Histogram of number of elements and skewness

53

3. Results and Discussion

The post-processing of the result data was done using COMSOL-Multiphysics®. For better visualization of results, three-time points were selected on the pressure pulse. The results presented below are consistent with the consideration of the Bertram et.al. (59) The following parameters were evaluated at time steps as described in Figure 35:

1. von Mises stress(N/m^2)
2. Pressure (Pa)
3. Darcy's Velocity (m/s)
4. Total displacement(mm)
5. Volumetric Strain

Figure 40 Time steps selected for visualization of results.

The above-mentioned parameters were evaluated for three different cases:

1. Poroelastic model of the spinal cord and the SAS with trabeculae
2. Poroelastic model of the spinal cord and the SAS without trabeculae
3. Poroelastic model of the spinal cord including the fourth ventricle without trabeculae.

55

3. Results and Discussion

Case 1: Poroelastic model of the spinal cord and the SAS with trabeculae

1. von Mises stress(N/m^2):

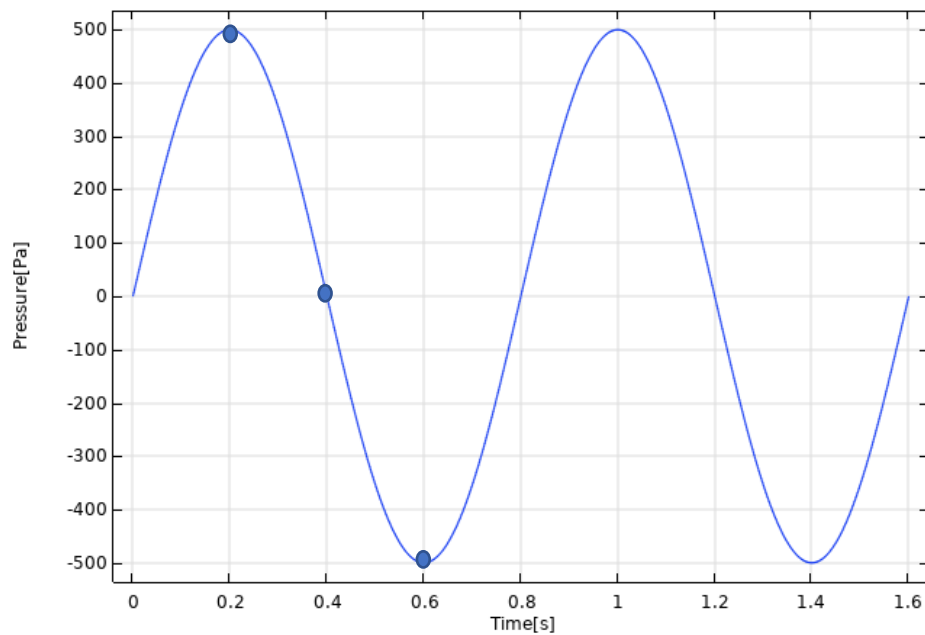The inclusion of trabeculae makes the spinal SAS poroelastic, which suggests some deformation in the spinal SAS as seen in the plots below. At a time-point of 0.2s where the pressure reaches to a maximum value of 500 Pa, the spinal cord tissue swells at the level of the syrinx. The 2D plot gives a clear view of boundary expansion by the spinal cord tissue into the syrinx. While at 0.4s of the pressure pulse, the deformation is zero. Later, at 0.6s, the spinal cord tissue seems to be compressed by the application of negative pressure i.e., -500 Pa. Considering the level of the syrinx, the pia mater at the region experience stresses of magnitude 10^3 N/m^2, for the highest and lowest amplitude of inlet pressure pulse. Stresses are also induced in dura mater along the length.

    I.   For time step: 0.2s
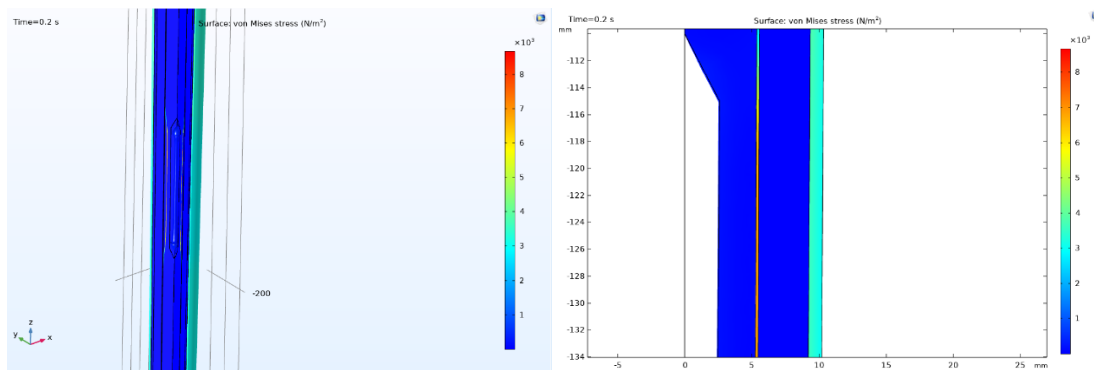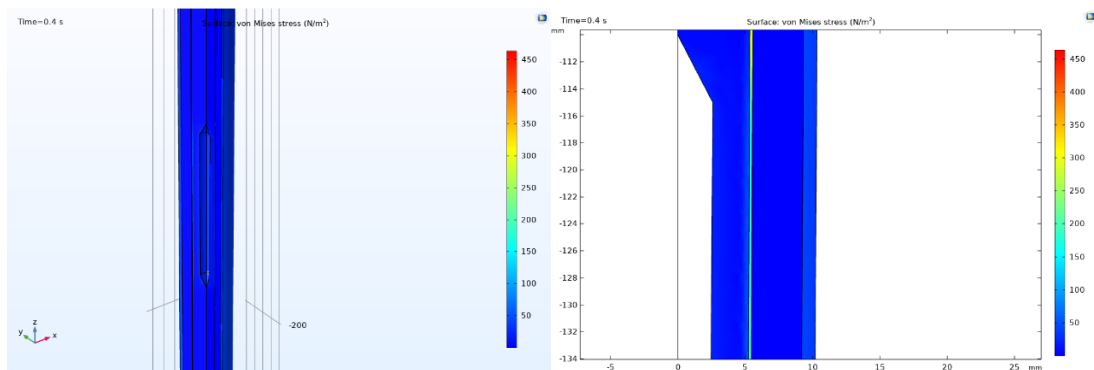
    II.   For time step: 0.4s

    III.   For time step: 0.6s
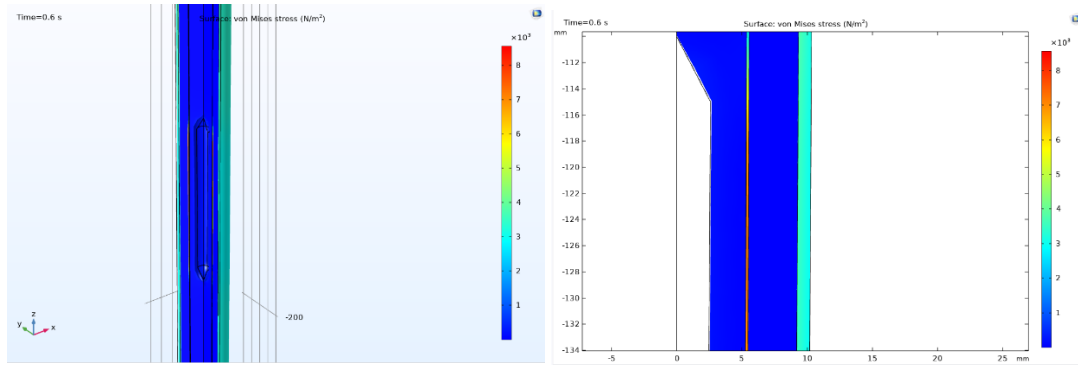
Figure 41 von Mises stress plotted in 3D and 2D model of the spinal cord at time-steps of 0.2s; 0.4s; 0.6s for Case 1.

2. Pressure (Pa):

Based upon the geometrical considerations, the following area (highlighted in blue), as shown in Figure 42, were chosen for extracting data in the form of point graphs to compare the results between the spinal SAS and the syrinx.
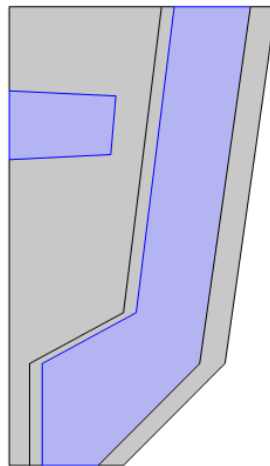
Figure 42 Model geometry depicting syrinx and SAS for visualization of results.

Pressure in Syrinx and SAS:

The wave propagation in the spinal SAS has the same amplitude as the inlet pressure pulse. The pressure wave observed in the syrinx has a maximum amplitude of 140 Pa. Pressure drop across the syrinx is significant as compared to the pressure in the SAS. Presence of a fluid filled cavity in the parenchyma surely reflects the pressure variation in the spinal cord. Hence an abnormal pattern is recorded in the syrinx as the pressure wave propagates in the SAS. As the pressure in SAS reaches +500 Pa, the pressure in the syrinx is 140 Pa. Meanwhile, when the pressure in the SAS is -500 Pa, the pressure in the syrinx is -130 Pa. The effect of caudal SAS pressure propagation due to change of material properties is reflected in the syrinx. Hence the pressure elevation in the syrinx is a larger fraction of the elevated caudal SAS pressure.
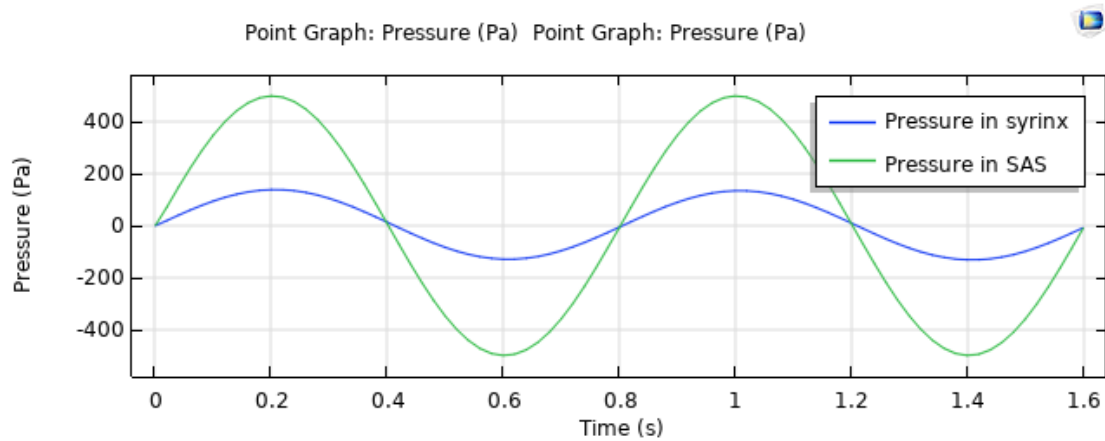
Figure 43 Plot of Pressure vs Time for Case 1

3. Darcy's Velocity (m/s)

A plot of Darcy's velocity in the syrinx and SAS is shown in the below figure. The magnitude of velocity in the syrinx varies as per the pressure wave propagation in the spinal cord. While the velocity magnitude in the SAS is 3×10^{-2} m/s, the velocity in the syrinx reaches highest amplitude of 7.7×10^{-4} m/s. The velocity profile reaches its highest values at systole and diastole with maximum pressure points. The initial values of the velocity shown in graph are a consequence of convergence artifact and the values stabilize later with time. As a matter of fact, the velocity is positive for majority of the cycle in radial direction, in varying magnitude which suggests the fluid rarely leaves the cord making it immersed in fluid at every periodic interval. Meanwhile, there is slightly negative velocity in the longitudinal direction when the pressure started to become negative.
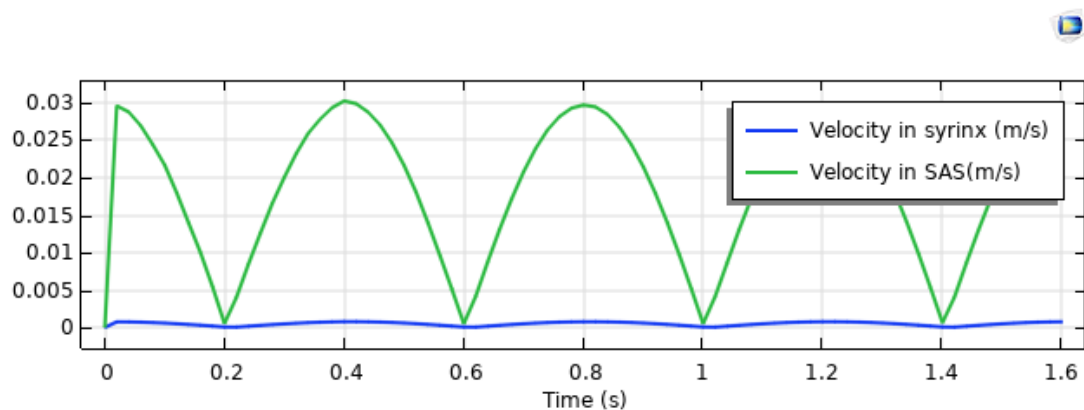
Figure 44 Plot of Darcy's velocity vs time for Case1

4. Total displacement(mm):

Displacement of the tissue at the syrinx-spinal cord boundary is greater than the displacement at the spinal cord-pia mater boundary. Periodic displacement is visible at the maximum pressure points. In fact, the displacement of the cord is dominant in the radial direction towards the dura mater, hence increasing and decreasing the size of the syrinx due to pore-flow interactions.
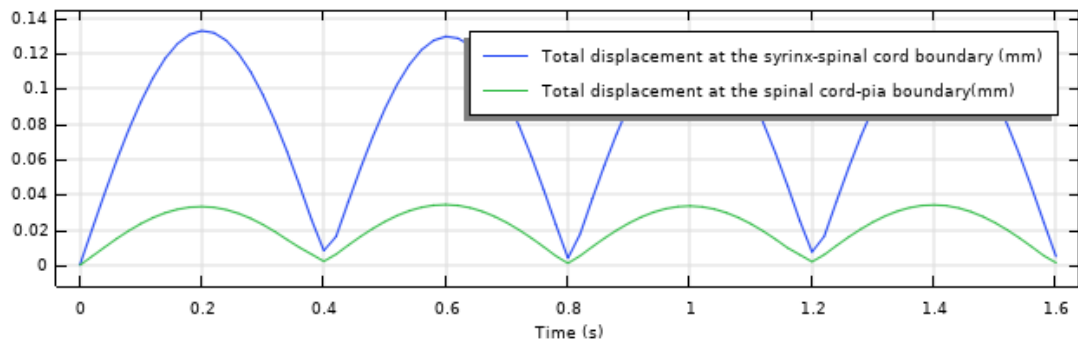
Figure 45 Plot of Total displacement vs time for Case 1

5. Volumetric Strain

Negative and positive values of volumetric strain suggestive of periodic compression and expansion of the spinal cord-pia boundary. The area under syrinx showcases periodic swelling, such condition exists due to differences in the seepage flowrates into and out of the cord and pia mater. The syrinx swells by 3.70% from a systole to the next diastole in volume in equispaced times through the defined cycle of excitation. As the pia is 250 times stiffer than the cord, fluid seepage in the pial tissue is small. Hence the interactions occur just before the cord/pia interface. The interactions are rather not in synchronisation with the inlet pressure wave. Tissue swelling occurs for a majority part of the pressure wave starting from systole to the start of diastole. Meanwhile, it shrinks creating a negative volumetric strain at the start of diastole. Furthermore, the amount of seepage going into the cord and coming out of it is comparatively not equal hence causing fluid retention into the cord.
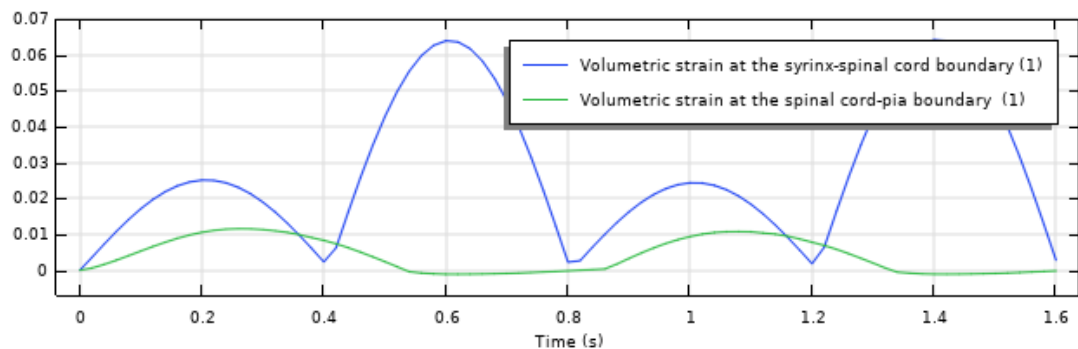
Figure 46 Plot of volumetric strain vs time for Case 1

CASE 2: Poroelastic model of the spinal cord and the SAS without trabeculae

1. von Mises stress(N/m^2)

The exclusion of trabeculae renders the spinal SAS as a fluid-filled cavity, which suggests no deformation in the spinal SAS as seen in the plots below. At a time-point of 0.2s where the pressure reaches to a maximum value of 500 Pa, no deformation is recorded in the spinal cord tissue at the level of the syrinx. The 2D plot gives a clear

view of the boundary condition by the spinal cord tissue and the syrinx. Considering the level of the syrinx, the pia mater at the region experience stresses of magnitude 10^2 N/m^2, for the highest and lowest amplitude of inlet pressure pulse.
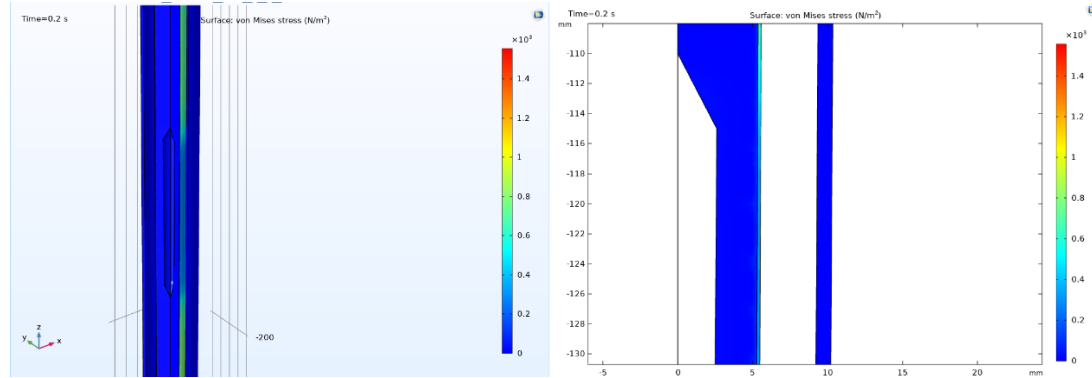
I.   For time step: 0.2s
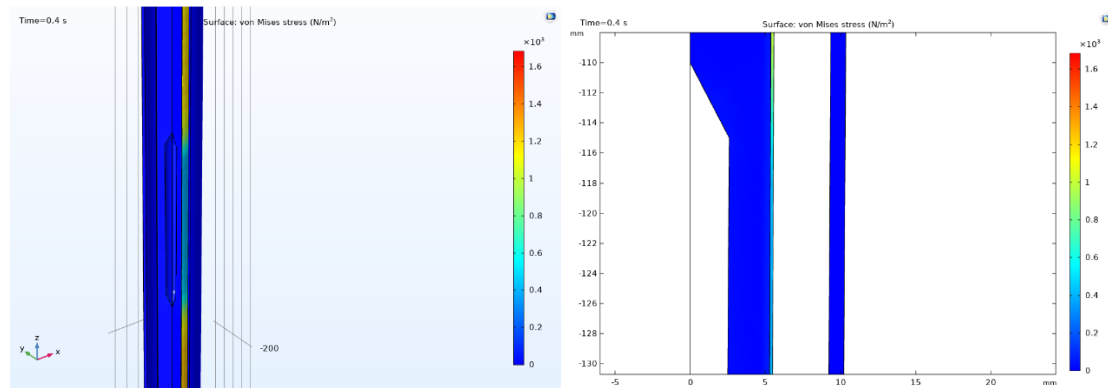
II.   For time step: 0.4s

III.   For time step: 0.6s
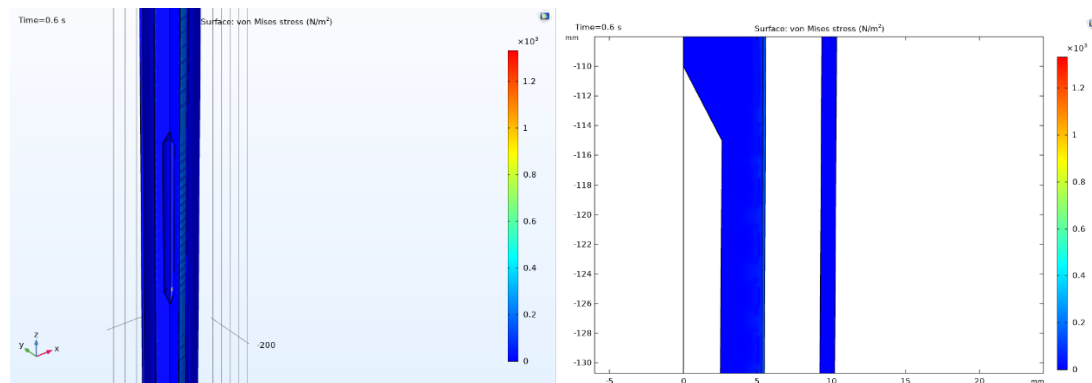
Figure 47 von Mises stress plotted in 3D and 2D model of the spinal cord at time-steps of 0.2s; 0.4s; 0.6s for Case 2.

2. Pressure (Pa)

The wave propagation in the spinal SAS has the same amplitude as the inlet pressure pulse. The SAS without the trabeculae acts as a fluid filled annular cylinder making the syrinx interactions infinitesimal. Hence the maximum pressure in the syrinx roughly reaches to 18 Pa. This suggests negligible interactions of the fluid in SAS and the

syrinx. The pressure elevation in the syrinx is significantly supplementary in the model with porous SAS than when it is nonporous.
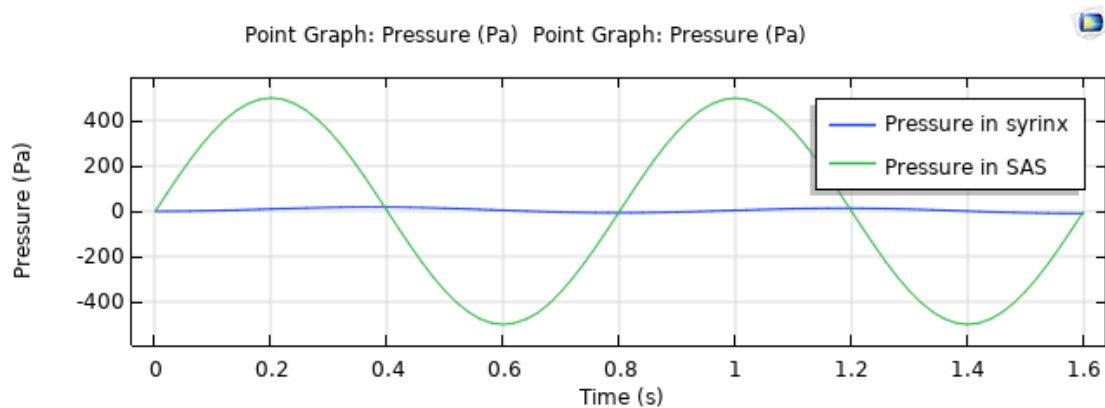
Figure 48 Plot of pressure vs time for Case 2

3. Darcy's Velocity (m/s)

The velocity profile in described in figure 49, shows irregular patterns corresponding to the inlet pressure wave. While it is expected that velocity is maximum at maximum pressure points. In this case, the velocity in the SAS is highest with value of 2.5×10^{-2} m/s, just before the reaching the maximum pressure points. Meanwhile, similar consequence is seen in the velocity profile of syrinx as well. A maximum value of 6.35×10^{-5} m/s is recorded in the syrinx at time point of 0.16s. Possible reason for this indiscretion is absence of resistance in the SAS as compared to case 1. On comparing the velocity recorded in both the SAS and the syrinx, the fluid seepage in the syrinx from the adjacent cord is infinitesimal.
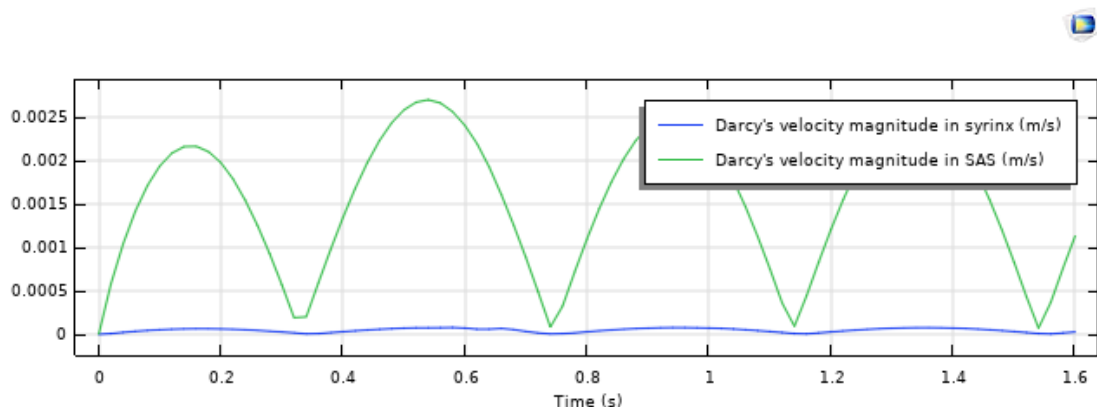
Figure 49 Plot of Darcy's velocity vs time for Case 2

4. Total displacement(mm)

The displacement of the syrinx/cord interface and the spinal/pia interface is approximately equal provided that there is drastic difference in the material properties of the spinal layers. The graph shown in fig. 50, records a growing displacement profile from the start of the cycle to the maximum pressure point of the systole. Meanwhile, at the start of diastole, for the rest of the part of the cycle the amplitude of the displacement

decreases significantly. Hence for the majority of the cycle the displacement is seen to be growing independent of the pressure propagation.
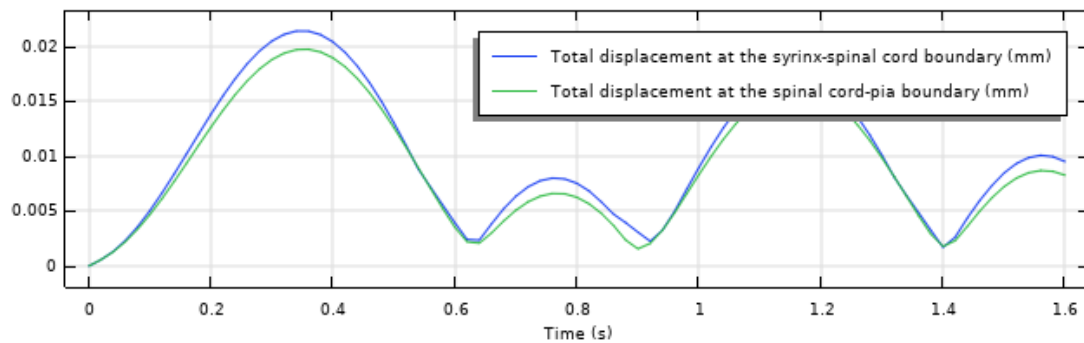
Figure 50 Plot of total displacement vs time for Case 2

5. Volumetric Strain in the syrinx

Negative and positive values of volumetric strain suggestive of periodic compression and expansion of the spinal cord-pia boundary. As a free-flowing channel is attached to the pial layer, the pia mater undergoes significant volumetric changes. The changes taking place are not in sync with the pressure wave propagation. Similar behaviour is recorded for the cord/syrinx interface, while the volumetric strain is positive for the entire cycle. Periodic expansion is not observed corresponding the pressure variation throughout the cycle. A cycle of expansion of the syrinx/cord boundary is observed from the start of the cycle to the maximum pressure point of the diastole. Another cycle of expansion occurs from a point just after the maximum pressure of the latter diastole to the start of next diastole. The change is volume in the syrinx is negligible as compared to the volume change quotient in Case 1. The pressure imposed due to the fluid in the SAS is compensated by the volumetric change in the pia/cord interface as major changes are observed at the deformation of the pia mater.
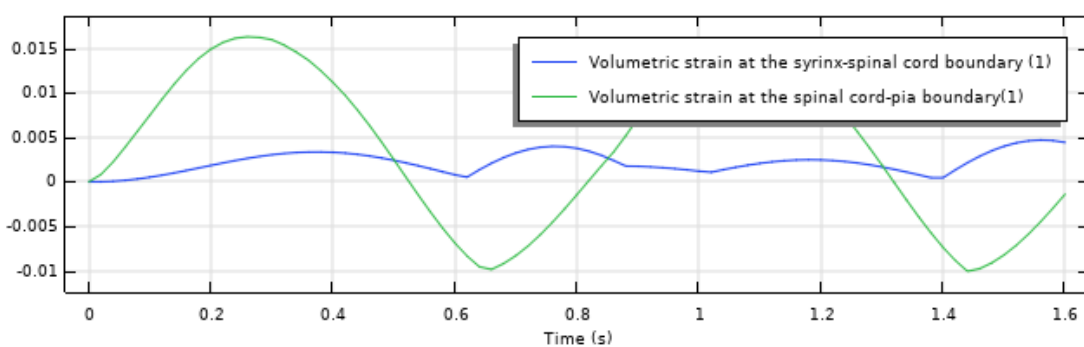
Figure 51 Plot of Volumetric strain vs time for Case 2

CASE 3: Poroelastic model of the spinal cord including the fourth ventricle.

Inlet at the roof of fourth ventricle shown in red
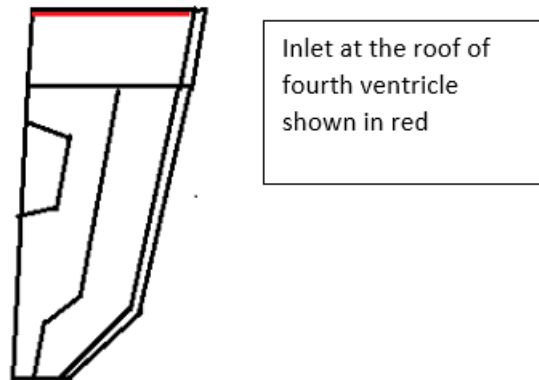
Figure 52 Schematic illustration of the inclusion of the fourth ventricle in the model geometry

1. von Mises stress(N/m^2)

The presence of the fourth ventricle at the top of the spinal cord and shifting the inlet boundary condition from the cranial end of the SAS to the roof of the fourth ventricle imposes different pressure conditions in the spinal cord. As described in Chapter 4, the pressure pulse with 700 Pa is applied at the roof of the fourth ventricle. At a time-point of 0.2s where the pressure reaches a maximum value of 700 Pa, the spinal cord tissue swells at the level of syrinx to a very small extent. While at 0.4s of the pressure pulse, the deformation is zero. Later, at 0.6s, the spinal cord tissue seems to be compressed by the application of negative pressure i.e., -700 Pa again to a small extent. Considering the level of the syrinx, the pia mater at the region experience stresses of magnitude 10^2 N/m^2, for the highest and lowest amplitude of inlet pressure pulse.
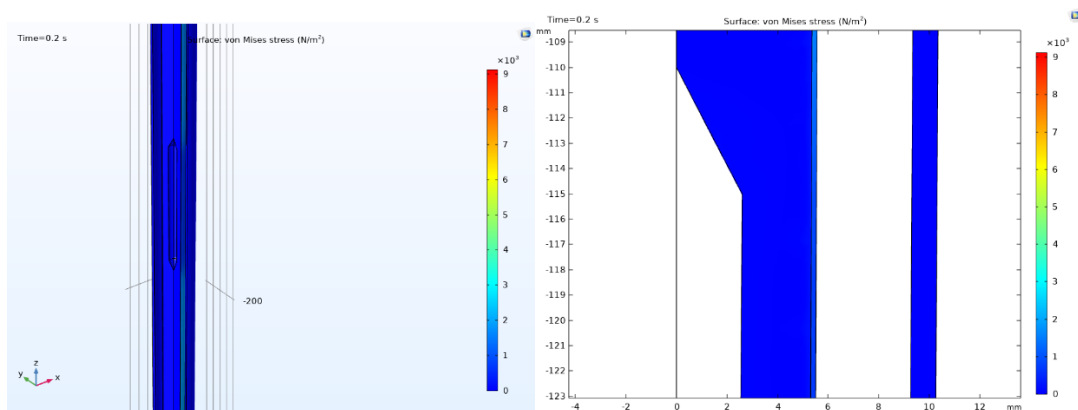
    I.   For time step: 0.2s
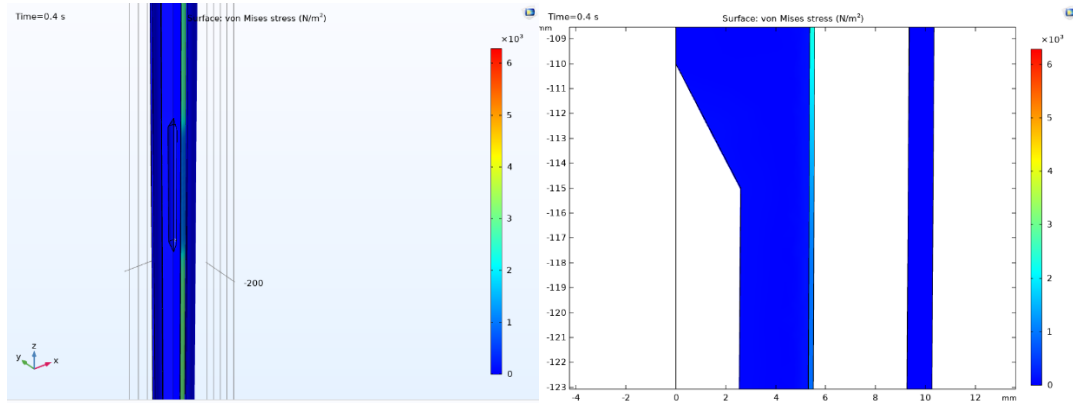
    II.   For time step: 0.4s

III.   For time step: 0.6s
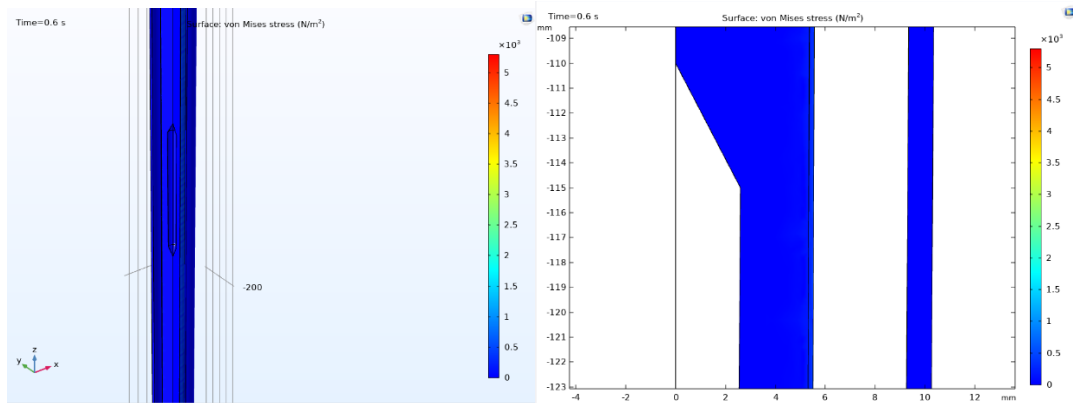
Figure 53 von Mises stress plotted in 3D and 2D model of the spinal cord at time-steps of 0.2s; 0.4s; 0.6s for Case 3.

2. Pressure (Pa)

The wave propagation in the spinal SAS has the same amplitude as the inlet pressure pulse. Pressure changes in case 3 is similar to Case 2. It is evident that the pressure in the syrinx is 25 Pa while the pressure in the SAS is 700 Pa. The overall axial and radial pressure change of the model in response to the pressure wave is entirely unaltered by the addition of the fourth ventricle geometry to the model.
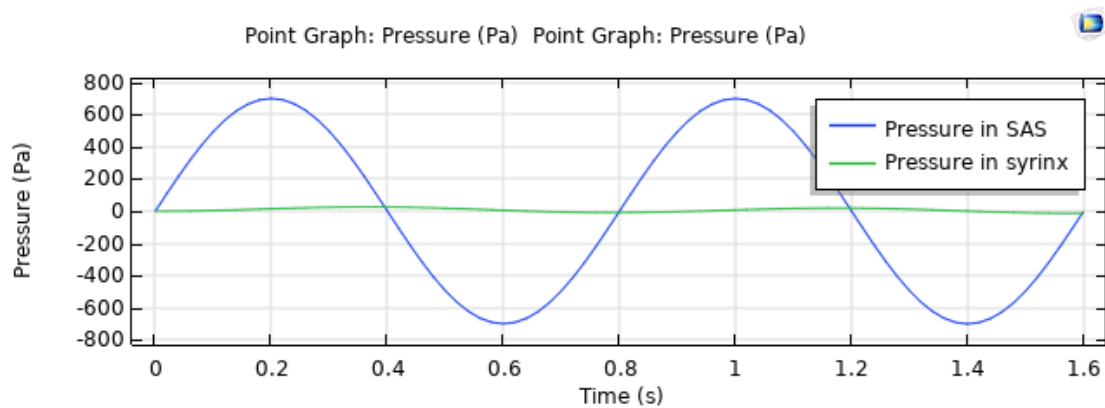
Figure 54 Plot of pressure vs time for Case 3

3. Darcy's Velocity (m/s) at the level of syrinx:

The velocity profile shows irregular patterns corresponding to the inlet pressure wave. While it is expected that velocity is maximum at maximum pressure. In this case the velocity is highest with value of 1×10^{-4} m/s, just before the pressure tend to maximum value. The velocity profile has similar behavior as compared to the case 2, respectively.
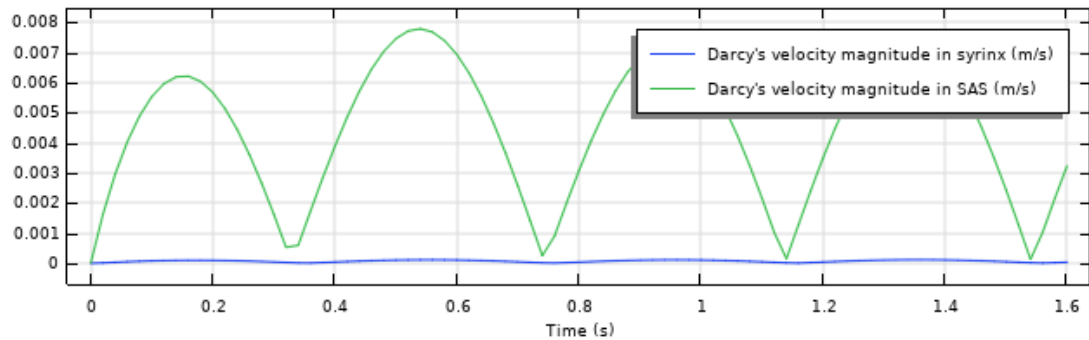
Figure 55 Plot of Darcy's velocity vs time for Case 3

4. Total displacement(mm)

While the pressure and velocity changes are minute in the model, the displacement is non negligible and follow an uneven pattern. The increasing and decreasing of tissue boundary in positive quotient is the effect of stresses induced in the pia mater and propagated in the cord and syrinx.
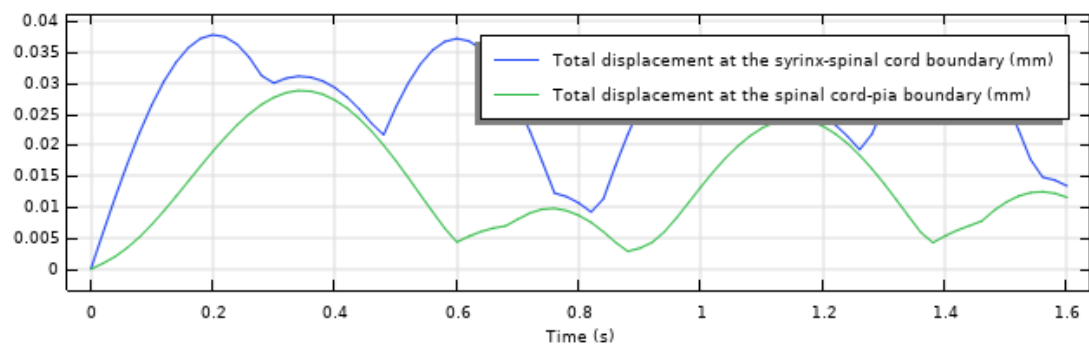
Figure 56 Plot of Total displacement vs time for Case 3

5. Volumetric Strain in the syrinx

Negative and positive values of volumetric strain suggestive of periodic compression and expansion of the spinal cord-pia boundary. While the cord/syrinx interface undergoes expansion in varying magnitude of strain values for the systolic part of the cycle. While the diastolic cycle causes negligible change in the volume of the syrinx. The complexities involved when trabeculae are existing in the model do not add to the processes taking place when the SAS is simply a fluid-filled cavity. Hence Darcy's law is inadequate to state the analysis when the SAS is non-porous.

3. Results and Discussion
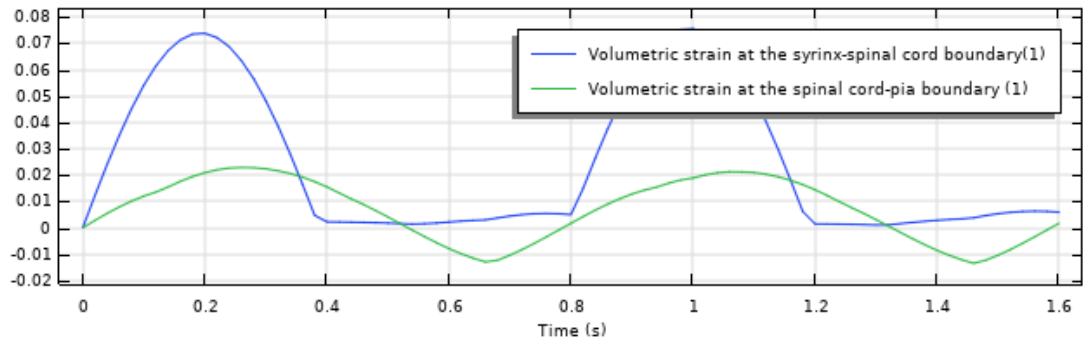
Figure 57 Plot of volumetric strain vs time for Case 3

4. Conclusion

The mathematical model of the spinal cord and adjoining tissues provide valuable insights into exploring the mechanism of syrinx formation. The main aim of this thesis was to study the effect of mechanical properties and flow dynamics on the spinal cord tissue with varying anatomical considerations. The focus was on modelling of intricate structures such as the trabeculae and the filum and its effects on the flow dynamics of the CSF. The simulation involved a pressure wave propagation in a 2D axis-symmetrical poroelastic model of the spinal cord in the presence of the syringomyelia.

In validation study, three different cases were analyzed to understand the effects of anatomical variations. The first case, a poroelastic model with trabeculae in the SAS. The main findings of the simulation for this particular case can be summarized as follows: A certain degree of periodic swelling and shrinkage exhibits at the syrinx level. At high pressure of 500 Pa, fluid enters the pores of the spinal cord tissue resulting in it to swell which can be inferred from the volumetric strains as well. Similarly, at a low pressure of -500 Pa, the fluid seeps through the porous cavities resulting in it to shrink. While the pressure inside the syrinx is lower than that of the SAS, it contradicts the theory put forth by Stoodley et al, (24). Gupta et al, (54), discussed the presence of trabeculae in the subarachnoid space is likely to inhibit the global deformation of the pia and arachnoid layers. A large stress concentration seen in the pia mater at the syrinx level can be due to deformations at syrinx from one side and resistance to the flow in the spinal subarachnoid space due to the trabecular network from another side. The second model, a poroelastic model without considering the trabecular network. The main findings were as follows: Although the syrinx cavity exhibits slight deformation based on the volumetric strain, the estimated deformations were small owing to the large parenchymal surface. The pressure and velocity fields inside the syrinx were much lower than the respective parameters of the Case 1 model. This causes little flow into the syrinx as most of the fluid is absorbed in the parenchyma. This complies with the study by Bertram and Heil, (59), where periodic swelling in the radial direction causes restricted flow in the syrinx. The third case, a poroelastic model including the fourth ventricle without a trabecular network. The main findings of the simulation for this case are as follows: Here again, the deformations are substantially lower than the deformations of Case 1, even though the pressure applied at the inlet was higher than that in Case 1. The presence of the fourth ventricle does not have a major impact on enlarging or reducing the syrinx cavity. This complies with a study by Martin et al. (47), that the fourth ventricle does not communicate freely with the syrinx. While the pressure in the syrinx was much lower than the spinal subarachnoid space. No stresses were induced at the dura mater, depicting that it acts as a wall for the fluid flow. The velocities in the radial direction are lesser than in the longitudinal direction.

In the computational study, the mathematical assumption for modelling of spinal cord tissue was applied for a 2D axisymmetric model. The incorporation of Darcy's law for pore-fluid interaction in the model proves effective in model with inclusion of trabeculae. As there is no free-flowing channel in model geometry, Darcy's equation stands valid for the processes. Meanwhile, the same for the model geometry without the inclusion of trabeculae does not stand valid as the SAS is considered as free flow fluid channel.

4. Conclusion

Although the parametric values appear to be much low corresponding to the parenchymal surface, the length and geometry might have affected the microscopic deformation as an abnormality is introduced in the system. As the model is uniform along the length, it is difficult to estimate the role of geometrical complexities such as cervical and lumbar enlargements. It is evident that the time-varying thickness of the cord, complexities due to addition of arachnoid trabeculae or the stenosis at the foramen magnum due to cerebellar herniation causes momentous changes in the CSF flow. Hence a patient-specific model will provide a good approximation to understand the role of geometry. The pressure values used during simulations were based on normal health conditions. The model has been more realistic if pressure calculated in vivo on CM patients was used as inlet condition. The material properties encountered throughout literature vary to a greater extent. The porosity of the spinal cord was chosen from an imaging study, but the value varies as used by most researchers. This may result in yielding different basis for the proposal of the theory of mechanics of the syrinx. As seen per the results, Darcy's law is simple in defining the flow of the CSF which is much more complex in reality. A definitive method to model the CSF flow and its interaction with the surrounding tissue will provide a realistic approximation towards the research in the Chiari-Syringomyelia disorder.

5. Fluid Structure Interaction

The poroelasticity gives a good insight into the interaction of the fluid with the porous solids, however, the complex flow of the CSF in the spinal SAS is not accounted for in Darcy's law. Darcy's law does not account for the viscous stresses in the interface between the solid and liquid phases when a free fluid zone is connected to the porous media. This is relevant in most biological cases. Furthermore, it does not provide a good approximation at the interface between the porous medium and the free fluid zone (68). While Brinkman's equations are an extension of Darcy's law and Navier- Stokes equation, provide a good approximation of pressure and velocity fields at the intersection of two domains (69); (70). These equations describe fast-moving fluids in porous media with the kinetic potential from fluid velocity, pressure, and gravity to drive the flow. These equations illustrate the transition between slow flow in porous media governed by Darcy's law and fast flow in channels described by the Navier-Stokes equations. The flow in porous media is governed by a combination of the continuity equation and the momentum equation, which together form the Brinkman equations:

$$\frac{\partial}{\partial t}(\varepsilon_p \rho) + \nabla \cdot (\rho \mathbf{u}) = Q_{br}$$

<div align="center">(Equation 6)</div>

$$\frac{\rho}{\varepsilon_p}\left(\frac{\partial \mathbf{u}}{\partial t} + (\mathbf{u} \cdot \nabla)\frac{\mathbf{u}}{\varepsilon_p}\right) =$$

$$-\nabla p + \nabla \cdot \left[\frac{1}{\varepsilon_p}\left\{\mu(\nabla \mathbf{u} + (\nabla \mathbf{u})^T) - \frac{2}{3}\mu(\nabla \cdot \mathbf{u})\mathbf{I}\right\}\right] - \left(\kappa^{-1}\mu + \frac{Q_{br}}{\varepsilon_p^2}\right)\mathbf{u} + \mathbf{F}$$

<div align="center">(Equation 7)</div>

The above equation consists of terms defined in Darcy's law with additional terms such as $\mathbf{Q}_{br}$ (SI unit: kg/(m^3·s)) is a mass source or mass sink; Influence of gravity and other volume forces can be accounted for via the force term $\mathbf{F}$ (SI unit: kg/(m^2·s^2)); ε_p is the porosity.

To study the effect of incorporating Brinkman's equation in the poroelastic model of the spinal cord, a fluid-structure interaction is implemented using COMSOL-Multiphysics® 5.5.

Fluid-Structure Interaction

A fluid-structure interaction model was developed as an extension of the poroelastic model to incorporate the complexities by using the Navier-Stokes equation while keeping the model geometry the same. A combination of Free and Porous Media Flow and Solid Mechanics was used to implement the physics. The free fluid flow in the spinal subarachnoid space was designed by replacing Darcy's law by the aforementioned equations. A mass source and body load were added to the poroelastic media in the model geometry, which serves as a coupling term. The poroelastic behavior of the solids was retained having the same properties described in Chapter 4. A physics-controlled surface mesh was generated with 85,999 mesh elements. Out of

which, 74031 are triangular elements, 4279 quadrilateral elements with three layers of boundary elements. A transient excitation pulse was applied at the cranial end of the spinal SAS of similar amplitude and frequency as described in Chapter 4. To aid the convergence criteria, an offset of 1000 Pa was added to the caudal end of the spinal SAS. The simulation has been performed for four cardiac cycles to eliminate the initial damping effects. The simulation took 20 hours to reach the convergence. The convergence criteria were set to relative tolerance of 0.01 and absolute tolerance of 10^{-3}.

Results and Discussion

The results were evaluated on four points at the level of the syrinx, on the following parameters:

1. von Mises stress(N/m^2)

In this model, negligible deformation is seen at the syrinx (points 3,4,8,10 on the syrinx geometry) (Figure 58) as compared to the dura mater (points 9,18,20 on the dura geometry) (Figure 59). It suggests that flow pressure causes maximum deformations in the dura and an insignificant amount of fluid passes through the spinal cord into the syrinx. As dura is elastic, it bulges from the center as the top and bottom parts are constrained.
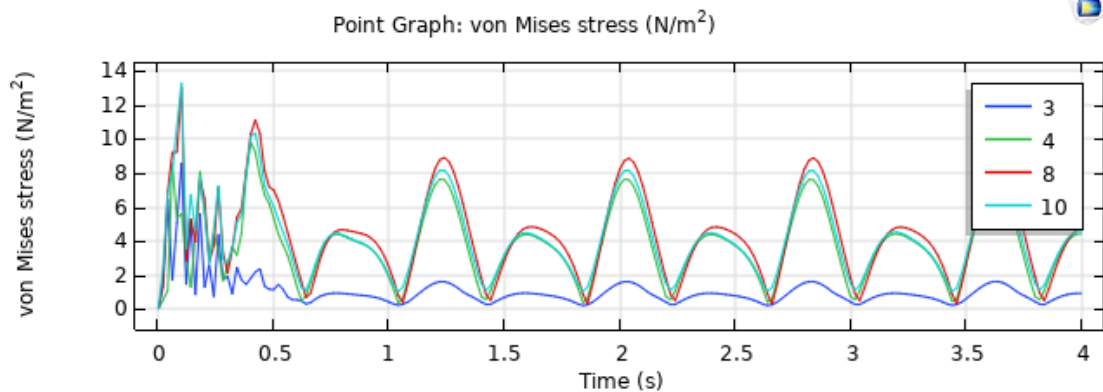
Figure 58 Plot of Von Mises stress vs time for Syrinx cavity
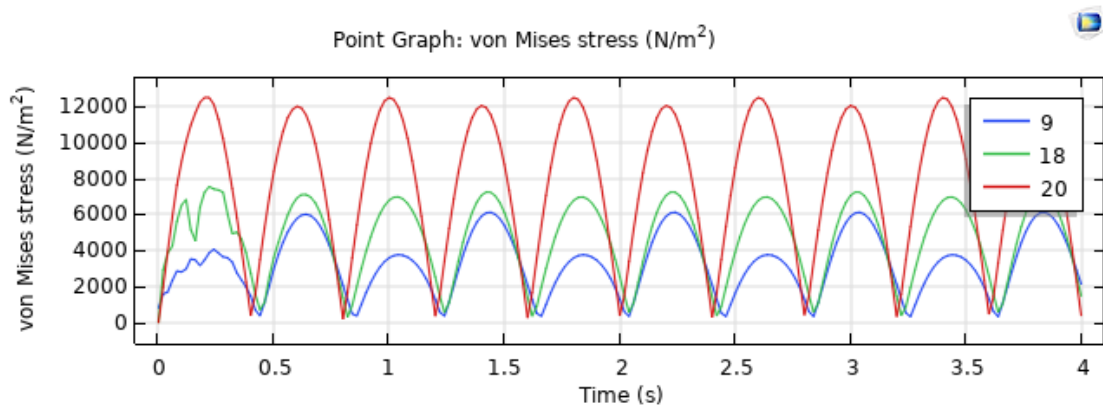
Figure 59 Plot of Von Mises stress vs time for Dura mater

5. Fluid Structure Interaction

2. Velocity (m/s)

Comparing (Figure 60) and (Figure 61), The velocities in the syrinx were considerably lower than in the SAS.

Figure 60 Plot of Velocity vs time for Syrinx cavity

Figure 61 Plot of Velocity vs time for the spinal SAS
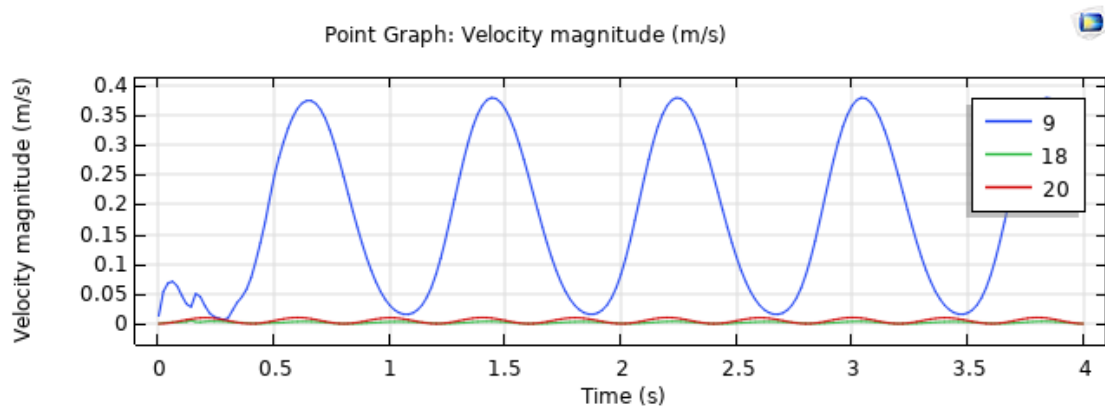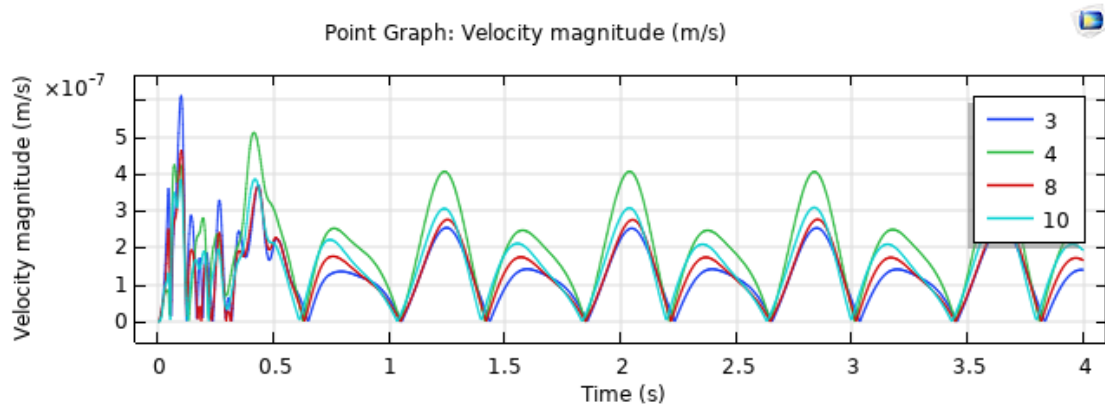
3.Pressure (Pa)

The trend is contradictory in case of pressure, as the syrinx has a pressure equal to the pressure in SAS.

Figure 62 Plot of Pressure vs time for Syrinx cavity
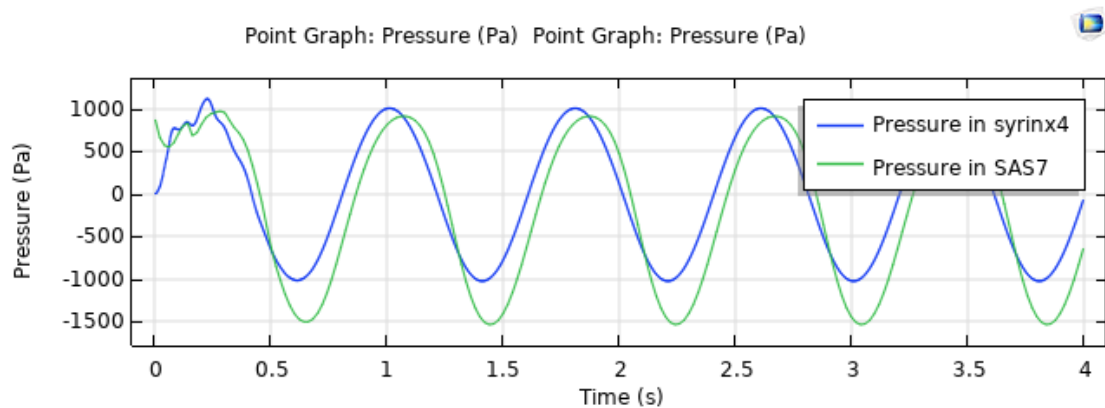
5. Fluid Structure Interaction

4. Volumetric strain

The compression and expansion of the syrinx cavity are peculiar with the trends seen in poroelastic models. The syrinx cavity appears to be moving in a longitudinal direction rather than compressing or expanding.
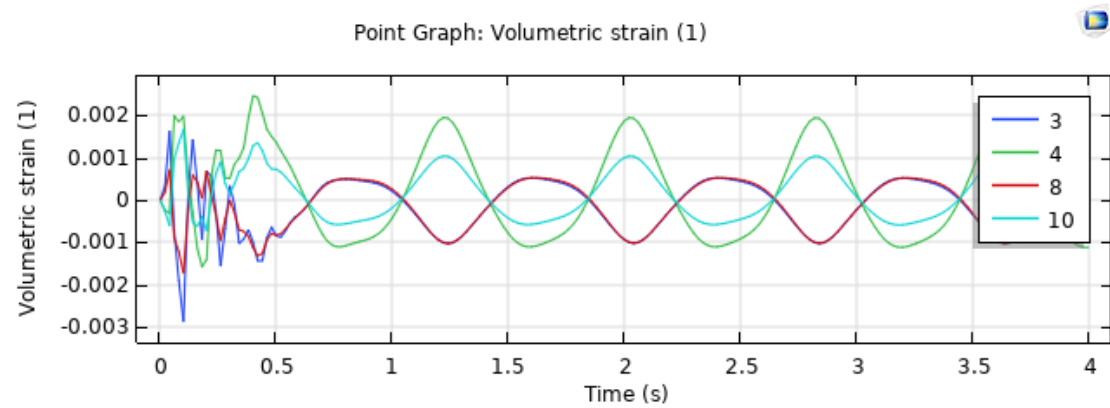
Figure 63 Plot of Volumetric strain vs time for Syrinx cavity

The fluid-structure interaction model provides a good start in analyzing the complex nature of the flow dynamics as it is capable of implementing suitable governing equations. Although higher computational costs make the method less efficient in terms of examining different material properties or boundary conditions.

References

1. **Sedzimir C, Roberts J, Occleshaw J et al.** *Gowers syringal haemorrhage-37:312–315.* s.l. : J Neurol Neurosurg Psychiatry, 1974.

2. **B, Williams.** *Post-traumatic syringomyelia.* s.l. : Paraplegia-28:296–313, 1990.

3. **Milhorat TH, Chou MW, Trinidad EM et al.** *Chiari 1 malformation redefined: clinical and radiographic findings .* s.l. : Neurosurgery- 44(5):1005, 1999.

4. **Elliott NSJ, Bertram CD, Martin BA et al.** *Syringomyelia: a review of the biomechanics.* s.l. : J Fluids Struct 40:1–24, 2013.

5. **Neary, A.R. Crossman and D.** *Neuroanatomy .* Manchester UK : Elsevier Limited, 2018.

6. **L Sakka, G Coll, J Chazal.** *Anatomy and physiology of cerebrospinal fluid.* s.l. : Eur Ann Otorhinolaryngol Head Neck Dis.2011 Dec;128(6):309-16, 2011.

7. **S. Jannesar, B. Nadler, and C. J. Sparrey.** *The Transverse Isotropy of Spinal Cord White Matter Under Dynamic Load.* s.l. : J. Biomech. Eng., vol. 138, no. 9, p. 091004, 2016.

8. **Y. Feng, R. J. Okamoto, R. Namani, G. M. Genin, and P. V. Bayly.** *Measurements of mechanical anisotropy in brain tissue and implications for transversely isotropic material models of white matter.* s.l. : J. Mech. Behav. Biomed. Mater., vol. 23, pp. 117–132, 2013.

9. **Fletcher, T. F.** Spinal Cord and Meninges.: Chapter 16 in Miller's Anatomy of the Dog, 2nd edition; ed. . s.l. : H. E. Evans and G. C. Christensen; W. B. Saunders Co, 1979.

10. **Darby, Gregory Cramer Susan.** *Clinical Anatomy of the Spine, Spinal Cord, and ANS-9780323082310.* s.l. : Mosby 2014, 2013.

11. **Parkinson, Gemma.** Structures of the Central Nervous System. *Neuroanatomy.* 2017.

12. **Yu, Justin Junehung.** *MECHANICAL PROPERTIES OF SPINAL CORD GREY MATTER AND WHITE MATTER IN CONFINED COMPRESSION.* Vancouver : B.A.Sc., University of Waterloo, 2015.

13. **Magdalena A. Lam, Sarah J. Hemley, Elmira Najafi, Nicole G. F. Vella, Lynne E. Bilston.** *The ultrastructure of spinal cord perivascular spaces: Implications for the circulation of cerebrospinal fluid.* s.l. : Scientific Reports-7: 12924 | DOI:10.1038/s41598-017-13455-4, 2017.

14. **E. T. ZHANG, C. B. E. INMAN AND R. WELLER.** *Interrelationships of the pia mater and the perivascular (Virchow-Robin) spaces in the human cerebrum.* s.l. : Anat. (1990), 170, 111-123.

15. **Bilston LE, Fletcher DF, Brodbelt AR et al.** *Arterial pulsation-driven cerebrospinal fl uid fl ow in the perivascular space .* s.l. : Computational Methods Biomech Biomed Engin 6(4):235–241, 2003.

16. **al., Martin M. Mortazavi et.** *Subarachnoid Trabeculae: A comprehensive review of their embryology, histology morphology and surgical significance.* s.l. : World Neurosurgery 10.1016/j.wneu.2017.12.041, 2017.

17. **Rickenbacher J, Landolt AM, Theiler K.** *Applied Anatomy of the Back .* s.l. : Berlin, Germany: Springer Science & Business Media; 2013:240.

18. **Scott G, Coats B.** *Micro-scale finite element modeling and optical coherence tomography imaging of the pia arachnoid complex. .* s.l. : Proceedings of the 17th U.S. National Congress on Theoretical and Applied Mechanics, East Lansing, Michigan,, 2014.

19. **Killer HE, Laeng HR, Groscurth P.** *Lymphatic capillaries in the meninges of the human optic nerve .* s.l. : J Neuroophthalmol. 1999;19:222-228.

20. **R. Shane Tubbs, W. Jerry Oakes.** *in Schmidek and Sweet Operative Neurosurgical Techniques (Sixth Edition), 2012.*

21. **Ozkan Tehli, Irgen Hodaj, Cahit Kural, Ilker Solmaz.** *Filum terminale .* s.l. : 2012 S. Karger AG, Basel 1016–2291/11/0476–0412$38.00/0.

22. **I G Bloomfield, I H Johnston, L E Bilston.** *Effects of proteins, blood cells and glucose on the viscosity of cerebrospinal fluid.* s.l. : Pediatr Neurosurg:1998 May;28(5):246-51. doi: 10.1159/000028659.

23. **Javed, Kinaan, Reddy, Vamsi and Lui., Forshing.** *Neuroanatomy, Choroid Plexus.* s.l. : -30844183, 2020.

24. **Brodbelt AR, Stoodley MA.** *CSF pathways: a review .* s.l. : Br J Neurosurg 21(5):510–520.

25. **Mauer UM, Freude G, Danz B et al.** *Cardiac gated phase-contrast magnetic resonance imaging of cerebrospinal fl uid fl ow in the diagnosis of idiopathic syringomyelia.* s.l. : Neurosurgery 63:1139–1144, 2008.

26. **Chang S, Wen S, Chen D et al.** *Small regulatory RNAs in neurodevelopmental disorders.* s.l. : Hum Mol Genet 18:R18–R26, 2008.

27. **Gard, Graham.** *An investigation into the regulation of intra-cranial pressure and its influence upon the surrounding cranial bone.* s.l. : Journal of Bodywork and Movement Therapies 13, 246–25, 2009.

28. **G. Flint, C. Rusbridge.** *Syringomyelia.* s.l. : DOI 10.1007/978-3-642-13706-8_20, © Springer-Verlag Berlin Heidelberg, 2014.

29. **H, Chiari.** *Ueber Veränderungen des Kleinhirns infolge von Hydrocephalie des Grosshirns. Dtsch Med infolge von Hydrocephalie des Grosshirns. Dtsch Med.*

30. **Lee J, Hida K, Seki T et al.** *(2003) Pierre-Robin syndrome associated with Chiari type I malformation. Childs Nerv Syst 19(5):380–383.*

31. **Atkinson JL, Kokmen E, Miller GM.** *(1998) Evidence of posterior fossa hypoplasia in the familial variant of adult Chiari I malformation: case report. Neurosurgery 42:401–403.*

32. **Cinalli G, Spennato P, Sainte-Rose C et al.** *(2005) Chiari malformation in craniosynostosis. Childs Nerv Syst 21(10):889–901. doi: 10.1007/s00381-004-1115-z.*

33. **Elisevich K, Fontaine S, Bertrand G.** *(1987) Syringomyelia as a complication of Paget's disease. J Neurosurg 66:611–613.*

34. **Meadows J, Kraut M, Guarnieri M et al.** *Asymptomatic Chiari type I malformations identified on magnetic resonance imaging. J Neurosurg 92(6):920–926.*

35. **Elyne N. Kahn, MD, Karin M. Muraszko.** *Prevalence of Chiari I Malformation and Syringomyelia.* s.l. : Neurosurg Clin N Am 26 (2015) 501–507.

References

36. **CODY A. DOBERSTEIN, BS, RADMEHR TORABI, MD and PETRA M. KLINGE, MD.** *Current Concepts in the Pathogenesis, Diagnosis, and Management of Type I Chiari Malformations.* s.l. : Rhode Island Medical Journal- 401-793- 9123.

37. **al., Faris Shweikeh et.** *National Trends, Complications, and Hospital Charges in Pediatric Patients with Chiari Malformation Type I Treated with Posterior Fossa Decompression with and without Duraplasty.* s.l. : 2015 S. Karger AG, Basel- 1016–2291/15/0000–0000$39.50/0.

38. **al., Rouleau GA et.** *Inherited occipital hypoplasia/syringomyelia in the cavalier King Charles spaniel: experiences in setting up a worldwide DNA collection 745–749. doi: 10.1093/jhered/esi074.* 2005.

39. **al., Fernandez AA et.** *Malformations of the craniocervical junction.* s.l. : BMC Musculoskelet Disord10(Suppl 1):S1.

40. **K Sivaramakrishna, K Sathyavaraprasad.** *Study on Syringomyelia.* s.l. : International Journal of Contemporary Medical Research 2017;4(10):2211-2214.

41. **Koyanagi I, Houkin K.** *Pathogenesis of syringomyelia associated with Chiari type 1 malformation: review of evidences and proposal of a new hypothesis.* s.l. : Neurosurg Rev 33:271–284.

42. **al., Oldfield EH et.** *Pathophysiology of syringomyelia associated with Chiari I malformation of the cerebellar tonsils Implications for diagnosis and treatment.* s.l. : J Neurosurg 80:3–15, 1994.

43. **JD, Heiss.** *Elucidating the pathophysiology of syringomyelia. .* s.l. : J Neurosurg 91:553–562, 1999.

44. **Heiss JD, Snyder K, Peterson MM.** *Pathophysiology of primary spinal syringomyelia.* s.l. : J Neurosurg Spine 17(5):367–380. doi: 10.3171/2012, 2012.

45. **al., Thompson et.** *Aetiology of herniation of the hindbrain in craniosyntosis :An investigation incorporating intracranial pressure monitoring and magnetic resonance imaging.* s.l. : Pediatr Neurosurg 26(6):288–295 , 2016.

46. **Wu T, Zhu Z.** *Syrinx resolution after posterior fossa decompression in patients with scoliosis secondary to Chiari malformation type I. Eur Spine J 21(6):1143–1150. doi: 10.1007/s00586-011-2064-3.*

47. **al., Martin et.** *Spinal Subarachnoid Space Pressure Measurements in an In Vitro Spinal Stenosis Model Implications on Syringomyelia Theories.* s.l. : Journal of Biomechanical Engineering-NOVEMBER 2010, Vol. 132 / 111007-1, 2010.

48. **Tubbs RS, et al.** *Institutional experience with 500 cases of surgically treated pediatric Chiari malformation Type I. J Neurosurg Pediatr 7(3):248–256.* 2011.

49. **al., Klekamp J et.** *A critical appraisal of syrinx cavity shunting procedures .* s.l. : J Neurosurg 89:382–388, 1997.

50. **Karlsson EK, Lindblad-Toh K.** *Leader of the pack: gene mapping in dogs and other model organisms .* s.l. : Nat Rev Genet 9:713–725, 2008.

51. **al., Drøsdal et.** *Effect of the Central Canal in the Spinal Cord on Fluid Movement within the Cord.* s.l. : The Neuroradiology Journal 26(5):585-90, 2013.

References

52. **al., Elizabeth C Clarke et.** *Computational fluid dynamics modelling of cerebrospinal fluid pressure in Chiari malformation and syringomyelia.* s.l. : J Biomech 2013 Jul 26;46(11):1801-9. doi: 10.1016/j.jbiomech.2013.05.013. Epub 2013 Jun 12, 2012.

53. **Karen H. Støverud, Hans Petter Langtangen, Victor Haughton, André Mardal.** *Poro-elastic modeling of Syringomyelia.* s.l. : Computer Methods in Biomechanics and Biomedical Engineering, DOI: 10.1080/10255842.2015.1058927.

54. **al., Sumeet Gupta et.** *Three-Dimensional Computational Modeling of Subject-Specific Cerebrospinal Fluid Flow in the Subarachnoid Space.* s.l. : Journal of Biomechanical Engineering-FEBRUARY 2009, Vol. 131 / 021010-1, 2009.

55. **al., Linge et.** *Characterization of Cyclic CSF Flow in the Foramen Magnum and Upper Cervical Spinal Canal with MR Flow Imaging and Computational Fluid Dynamics.* s.l. : American Journal of Neuroradiology 31(6):997-1002, 2011.

56. **Vartan Kurtcuoglu, Kartik Jain, and Bryn A. Martin.** *Modelling of Cerebrospinal Fluid Flow by Computational Fluid Dynamics.* s.l. : Biomedical Engineering, https://doi.org/10.1007/978-3-030-04996-6_9, 2019.

57. **Martin BA, Loth F.** *The influence of coughing on cerebrospinal fluid pressure in an in vitro syringomyelia model with spinal subarachnoid space stenosis.* s.l. : Cerebrospinal Fluid Research volume 6, Article number: 17 (2009), 2009.

58. **D., Bertram C.** *Evaluation by Fluid/Structure Interaction Spinal-Cord Simulation of the Effects of Subarachnoid-Space Stenosis on an Adjacent Syrinx.* s.l. : Journal of Biomechanical Engineering-JUNE 2010, Vol. 132 / 061009-1, 2010.

59. **Heil, C. D. Bertram and M.** *A Poroelastic Fluid/Structure Interaction Model of Cerebrospinal Fluid Dynamics in the Cord With Syringomyelia and Adjacent Subarachnoid-Space Stenosis.* s.l. : Journal of Biomechanical Engineering-JANUARY 2017, Vol. 139 / 011001-1, 2017.

60. **Harris PJ, Hardwidge C.** *A porous finite element model of the motion of the spinal cord.* . s.l. : n: Constanda C, Pérez ME (eds) Integral methods in science and engineering, vol 2, Computational methods. Birkhäuser Boston, pp 193–201, 2010.

61. **al., Moeendarbary et.** *The cytoplasm of living cells behaves as a poroelastic material.* s.l. : NATURE MATERIALS | VOL 12- :10.1038/NMAT3517, 2013.

62. **Bear, J.** *Hydraulics of Groundwater, McGraw-Hill, 1979.*

63. **N.H. Sleep and K. Fujita.** *Principles of Geophysics, Blackwell Science, 1997.*

64. **Sanford, S.E. Ingebritsen and W.E.** *Groundwater in Geologic Processes, Cambridge University Press, 1998.*

65. **al., Hui Zhang et.** *NODDI: Practical in vivo neurite orientation dispersion and density imaging of the human brain.* s.l. : -10.1016/j.neuroimage.2012.03.072, 2012.

66. **Assaf, Y., Cohen, Y.** *Assignment of the water slow-diffusing component in the central nervous system using q-space diffusion MRS: implications for fiber tract imaging.* s.l. : Magn. Reson. Med. 43, 191–199 , 2000.

67. **Williams, B.** *Simultaneous Cerebral and Spinal Fluid Pressure Recordings.* s.l. : by Springer-Verhg 1981, 1981.

References

68. **Vafai., A. R A Khaled and K.** *"The role of porous media in modeling flow and heat transfer in biological tissues". In: International Journal of Heat and Mass Transfer 46.26 (2003),*. s.l. : pp. 4989–5003. ISSN: 00179310. DOI:.

69. **Bejan, D. Nield and A.** *Convection in Porous Media, 3rd ed., Springer, 2006.*

70. **Worster, M. Le Bars and M.G.** *"Interfacial Conditions Between a Pure Fluid and a Porous Medium: Implications for Binary Alloy Solidification," J. of Fluid Mechanics, vol. 550, pp. 149–173, 2006.*

72. **Le, E. Hanh.** *The Healthline Medical Network.* 2018.

73. **Derrickson, Tortora and Derrickson and Bryan.** *ANATOMY & PHYSIOLOGY.* s.l. : ohn Wiley & Sons, Inc-978-1-118-34500-9 , 2014.

74. **Lane, Rona F. Woldenberg and Elizabeth L.** *Encyclopedia of the Neurological Sciences.* 2003.

75. **Low, Miles W. Cloyd Frank N.** *Scanning electron microscopy of the subarachnoid space in the dog. I. Spinal cord levels.* s.l. : John Wiley & Sons, Inc-/10.1002/cne.901530402, 1974.

76. **Trigylidas T, Baronia B, Vassilyadi M, Ventureyra.** *(2008) Posterior fossa dimension and volume estimates in pediatric patients with Chiari I malformation .* s.l. : Childs Nerv Syst 24(3):329–336.

77. **Klekamp J, Iaconetta G.** *Syringomyelia associated with foramen magnum arachnoiditis.* s.l. : J Neurosurg 97(3 Suppl):317–322, 2002.